The Astrophysical Journal, 742:59 (19pp), 2011 November 20 doi:10.1088/0004-637X/742/1/59

HAT-P-32b AND HAT-P-33b: TWO HIGHLY INFLATED HOT JUPITERS TRANSITING HIGH-JITTER STARS*

J. D. Hartman[1], G. Á. Bakos[1], G. Torres[1], D. W. Latham[1], Géza Kovács[2], B. Béky[1], S. N. Quinn[1], T. Mazeh[3], A. Shporer[4,5], G. W. Marcy[6], A. W. Howard[6], D. A. Fischer[7], J. A. Johnson[8], G. A. Esquerdo[1], R. W. Noyes[1], D. D. Sasselov[1], R. P. Stefanik[1], J. M. Fernandez[9], T. Szklenár[1], J. Lázár[10], I. Papp[10], and P. Sári[10]
[1] Harvard-Smithsonian Center for Astrophysics, Cambridge, MA, USA; gbakos@cfa.harvard.edu
[2] Konkoly Observatory, Budapest, Hungary
[3] School of Physics and Astronomy, Raymond & Beverly Sackler Faculty of Exact Sciences, Tel Aviv University, Tel Aviv 69978, Israel
[4] LCOGT, 6740 Cortona Drive, Santa Barbara, CA, USA
[5] Department of Physics, Broida Hall, University of California, Santa Barbara, CA, USA
[6] Department of Astronomy, University of California, Berkeley, CA, USA
[7] Department of Astronomy, Yale University, New Haven, CT, USA
[8] Department of Astrophysics, California Institute of Technology, Pasadena, CA, USA
[9] Georg-August-Universität Göttingen, Institut für Astrophysik, Göttingen, Germany
[10] Hungarian Astronomical Association, Budapest, Hungary
Received 2011 June 6; accepted 2011 September 28; published 2011 November 3

ABSTRACT

We report the discovery of two exoplanets transiting high-jitter stars. HAT-P-32b orbits the bright $V = 11.289$ late-F–early-G dwarf star GSC 3281-00800, with a period $P = 2.150008 \pm 0.000001$ d. The stellar and planetary masses and radii depend on the eccentricity of the system, which is poorly constrained due to the high-velocity jitter ($\sim$80 m s^{-1}). Assuming a circular orbit, the star has a mass of $1.16 \pm 0.04\,M_\odot$ and radius of $1.22 \pm 0.02\,R_\odot$, while the planet has a mass of $0.860 \pm 0.164\,M_J$ and a radius of $1.789 \pm 0.025\,R_J$. The second planet, HAT-P-33b, orbits the bright $V = 11.188$ late-F dwarf star GSC 2461-00988, with a period $P = 3.474474 \pm 0.000001$ d. As for HAT-P-32, the stellar and planetary masses and radii of HAT-P-33 depend on the eccentricity, which is poorly constrained due to the high jitter ($\sim$50 m s^{-1}). In this case, spectral line bisector spans (BSs) are significantly anti-correlated with the radial velocity residuals, and we are able to use this correlation to reduce the residual rms to $\sim$35 m s^{-1}. We find that the star has a mass of $1.38 \pm 0.04\,M_\odot$ and a radius of $1.64 \pm 0.03\,R_\odot$ while the planet has a mass of $0.762 \pm 0.101\,M_J$ and a radius of $1.686 \pm 0.045\,R_J$ for an assumed circular orbit. Due to the large BS variations exhibited by both stars we rely on detailed modeling of the photometric light curves to rule out blend scenarios. Both planets are among the largest radii transiting planets discovered to date.

Key words: planetary systems – stars: individual (HAT-P-32, GSC 3281-00800, HAT-P-33, GSC 2461-00988) – techniques: photometric – techniques: spectroscopic

Online-only material: color figures, machine-readable tables

1. INTRODUCTION

One of the most significant findings that has resulted from the study of transiting exoplanets (TEPs) over the past decade is the discovery that some close-in "hot Jupiters" have radii that are substantially larger than what was thought to be theoretically possible. The three most inflated TEPs, including WASP-17b ($R = 1.99 \pm 0.08\,R_J$; Anderson et al. 2011), WASP-12b ($R = 1.79 \pm 0.09\,R_J$; Hebb et al. 2009), and TrES-4b ($R = 1.78 \pm 0.09\,R_J$; Sozzetti et al. 2009) have radii that are as much as 50% larger than expected from, for example, the coreless Fortney et al. (2007) models. Recently, it has become clear that the degree to which TEPs are inflated is correlated with the planet equilibrium temperature (Fortney et al. 2007; Enoch et al. 2011; Kovács et al. 2010; Faedi et al. 2011; Béky et al. 2011; Laughlin et al. 2011) and anti-correlated with stellar metallicity (Guillot et al. 2006; Fortney et al. 2007; Burrows et al. 2007; Enoch et al. 2011; Béky et al. 2011). Several mechanisms that might explain the correlation with equilibrium temperature in particular have been proposed (Bodenheimer et al. 2001; Guillot & Showman 2002; Batygin and Stevenson 2010), though to date this issue remains unresolved.

In this work, we report the discovery of two new TEPs, HAT-P-32b and HAT-P-33b (orbiting the stars GSC 3281-00800 and GSC 2461-00988, respectively), with radii among the largest found to date. These planets have high equilibrium temperatures, supporting the aforementioned correlation. Both of these highly inflated hot Jupiters were discovered by the Hungarian-made Automated Telescope Network (HATNet; Bakos et al. 2004) survey for TEPs orbiting bright stars ($9 \lesssim r \lesssim 14.5$). HATNet operates six wide-field instruments, including four at the Fred Lawrence Whipple Observatory (FLWO) in Arizona, and two on the roof of the hangar servicing the Smithsonian Astrophysical Observatory's Submillimeter Array in Hawaii.

Although the two planets presented here were among the first candidates identified by HATNet, with discovery observations dating back to 2004, they proved to be difficult to confirm due to the significant radial velocity (RV) jitter exhibited by the stellar hosts (78.7 m s^{-1} and 55.1 m s^{-1} for HAT-P-32 and HAT-P-33, respectively), which limits the power of the traditional spectral line bisector technique used to rule out blend scenarios. We argue that the jitter is astrophysical in origin, and likely related to convective inhomogeneities which vary in time, perhaps due to time-varying photospheric magnetic fields, and we conduct detailed blend modeling of the observations to confirm the planetary nature of these systems. The high jitter values for

* Based in part on observations obtained at the W. M. Keck Observatory, which is operated by the University of California and the California Institute of Technology. Keck time has been granted by NOAO (A285Hr, A146Hr, A201Hr, A289Hr), NASA (N128Hr, N145Hr, N049Hr, N018Hr, N167Hr, N029Hr), and the NOAO Gemini/Keck time-exchange program (G329Hr).

Table 1
Summary of Photometric Observations

Instrument/Field	Date(s)	Number of Images[a]	Mode Cadence (s)	Filter
HAT-P-32				
HAT-7/G125	2005 Sep–2006 Feb	7077	330	*I* band
HAT-8/G125	2005 Sep–2005 Oct	816	330	*I* band
HAT-6/G126	2004 Dec–2005 Mar	1365	330	*I* band
HAT-9/G126	2004 Dec–2005 Mar	1505	330	*I* band
KeplerCam	2007 Sep 24	602	33	*z* band
KeplerCam	2007 Oct 22	489	53	*z* band
KeplerCam[b]	2007 Oct 23	161	38	*z* band
KeplerCam	2007 Nov 6	759	28	*z* band
KeplerCam[b]	2007 Nov 18	551	38	*z* band
KeplerCam	2007 Nov 19	665	38	*z* band
KeplerCam[b]	2007 Dec 3	817	33	*z* band
KeplerCam	2007 Dec 4	596	33	*g* band
HAT-P-33				
HAT-6/G176	2004 Nov–2005 Oct	2754	330	*I* band
HAT-9/G176	2004 Nov–2005 Oct	4383	330	*I* band
WHAT/G221	2004 Jan–2005 May	5439	330	*I* band
KeplerCam	2006 Dec 29	413	33	*i* band
KeplerCam	2007 Nov 24	274	57	*z* band
KeplerCam	2008 Mar 25	260	29	*z* band
KeplerCam	2008 Nov 23	668	28	*i* band
KeplerCam	2008 Nov 30	257	32	*i* band
KeplerCam	2011 Feb 14	346	57	*g* band
KeplerCam	2011 Feb 21	336	58	*g* band

Notes.
[a] For HATNet and WHAT observations this includes images which were rejected by the photometric reduction pipeline. For KeplerCam observations this excludes images which were rejected by the photometric reduction pipeline, but includes images which were rejected via σ-clipping during the fitting procedure.
[b] Out-of-transit observation used to constrain the presence of a secondary transit event during blend modeling.

both stars result in poor constraints on the orbital eccentricities of the two systems. We model the systems both assuming circular orbits and allowing the eccentricity to vary. Given the lack of definite evidence for non-zero eccentricities, for applications requiring a single set of parameters for each system we provisionally suggest adopting the circular orbit parameters. However, we note that several eccentric short-period TEPs have been discovered (e.g., XO-3b, Johns-Krull et al. 2008; WASP-14b, Joshi et al. 2009; HAT-P-21b, Bakos et al. 2011), so assuming circular orbits may thus underestimate the true parameter uncertainties. We consider both eccentric and circular cases throughout the paper. Importantly the inferred planetary radii depend strongly on the orbital eccentricities. In particular, if HAT-P-32b has an eccentric orbit, its radius may be larger than any other known TEP.

The structure of the paper is as follows. In Section 2, we summarize the detection of the photometric transit signal and the subsequent spectroscopic and photometric observations of each star to confirm the planets. In Section 3, we analyze the data to rule out false positive scenarios and to determine the stellar and planetary parameters. Our conclusions are discussed in Section 4.

2. OBSERVATIONS

2.1. Photometric Detection

Table 1 summarizes the HATNet discovery observations of each new planetary system. The HATNet images were processed and reduced to trend-filtered light curves following the procedure described by Bakos et al. (2010). The light curves were searched for periodic box-shaped signals using the Box Least-Squares (see Kovács et al. 2002) method. For HAT-P-33, supporting observations of the discovery were obtained with the Wise-HAT (WHAT; Shporer et al. 2009) telescope at Wise Observatory in Israel; these were analyzed in the same manner as the HATNet images. We detected significant signals in the light curves of the stars summarized below.

1. *HAT-P-32*. GSC 3281-00800 (also known as 2MASS 02041028+4641162; $\alpha = 02^{\rm h}04^{\rm m}10\overset{\rm s}{.}27$, $\delta = +46^\circ41'16\overset{''}{.}2$; J2000; $V = 11.289$; Droege et al. 2006). A signal was detected for this star with an apparent depth of ~20.3 mmag and a period of $P = 2.1500$ d (see Figure 1, left).
2. *HAT-P-33*. GSC 2461-00988 (also known as 2MASS 07324421+3350061; $\alpha = 07^{\rm h}32^{\rm m}44\overset{\rm s}{.}20$, $\delta = +33^\circ50'06\overset{''}{.}2$; J2000; $V = 11.188$; Droege et al. 2006). A signal was detected for this star with an apparent depth of ~8.5 mmag and a period of $P = 3.4745$ d (see Figure 1, right).

2.2. Reconnaissance Spectroscopy

High-resolution, low signal-to-noise ratio (S/N) "reconnaissance" spectra were obtained for both HAT-P-32 and HAT-P-33 using the Harvard-Smithsonian Center for Astrophysics (CfA) Digital Speedometer (DS; Latham 1992) on the FLWO 1.5 m telescope. These observations, which are summarized in Table 2, were reduced and analyzed following the procedure described by Torres et al. (2002) (see also Latham et al. 2009). We find that both stars show no velocity variation at the 1 km s^{-1} precision of the observations, and all spectra are consistent with

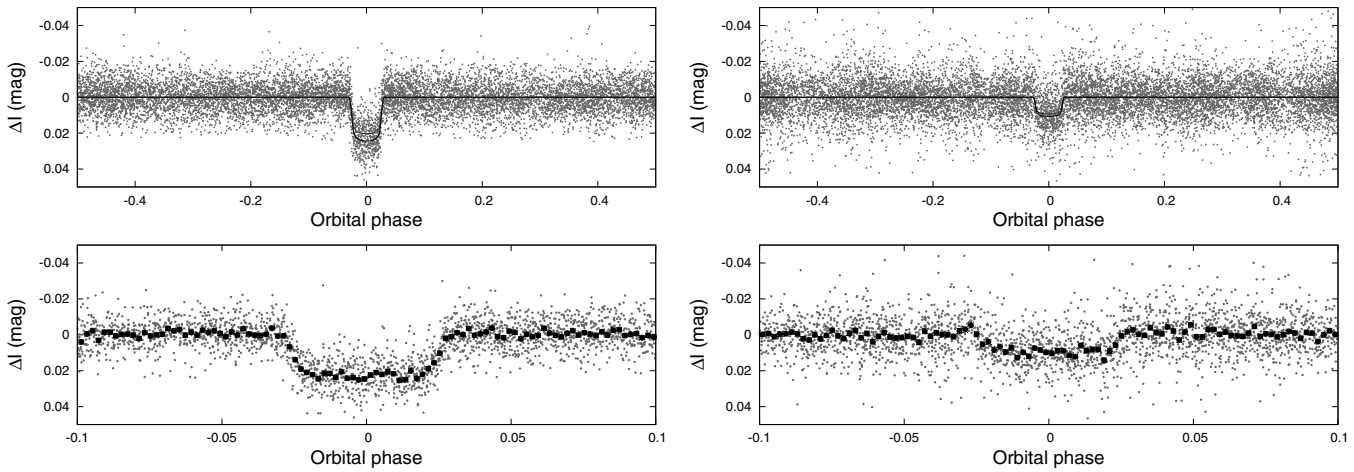

Figure 1. Left: unbinned light curve of HAT-P-32 from HATNet (top, see the text for details), folded with the period $P = 2.1500085$ d. The solid line shows a transit-model fit to the light curve (Section 3.4). We also show a zoomed-in view of the transit (bottom), with the dark points showing the light curve binned in phase with a bin size of 0.002 (∼6.2 minutes for HAT-P-32 and 10 minutes for HAT-P-33). Right: same as left—here we show HAT-P-33.

Table 2
DS Reconnaissance Spectroscopy Observations

JD – 2,400,000	RV[a] (km s^{-1})	σ_{RV}[b] (km s^{-1})
HAT-P-32		
53988.0008	−24.58	1.37
53992.9400	−24.02	1.05
54016.7473	−23.51	0.75
54070.7298	−23.80	1.08
54072.7003	−24.07	0.71
54075.8081	−22.86	0.62
54077.7263	−23.25	0.75
54421.8025	−21.91	0.81
54422.7370	−23.67	0.92
54423.7596	−23.03	0.86
54424.7471	−23.80	0.78
54425.8210	−22.60	0.77
54427.7552	−22.34	1.00
54430.6748	−20.83	1.70
54726.8681	−23.50	0.90
HAT-P-33		
53864.6428	22.10	0.62
53865.6274	21.91	0.48
53866.6480	22.41	0.48
53873.6285	24.07	0.63
54041.9844	23.21	0.76
54043.9879	24.41	0.79
54047.0178	22.75	0.64
54047.9772	23.54	0.50
54048.9252	22.84	0.66

Notes.
[a] The measured heliocentric RV of the target quoted on the native CfA system. Our best guess is that 0.14 km s^{-1} should be added to put the CfA velocities onto an absolute system defined by observations of minor planets.
[b] The RV measurement uncertainty.

single, moderately rotating dwarf stars. For HAT-P-32, the stellar atmospheric parameters that we find, assuming solar composition, are $T_{\rm eff\star} = 6500 \pm 100$ K, $\log g_\star = 4.5 \pm 0.25$, $v \sin i = 21.9 \pm 1.0$ km s^{-1}, and $\gamma_{\rm RV} = -23.21 \pm 0.26$ km s^{-1}. For HAT-P-33, we find $T_{\rm eff\star} = 6500 \pm 100$ K, $\log g_\star = 4.0 \pm 0.25$, $v \sin i = 15.6 \pm 1.0$ km s^{-1}, and $\gamma_{\rm RV} = 23.03 \pm 0.28$ km s^{-1}.

In addition to the DS observations for HAT-P-33, we also obtained several initial reconnaissance observations of this target with the SOPHIE spectrograph on the Observatoire de Haute-Provence 1.93 m telescope. These observations showed ∼100 m s^{-1} scatter, with only a very faint hint of phasing with the photometric ephemeris, hinting at the possibility that the system is a blend. Based on these observations we postponed further follow-up of the target for several years.

2.3. High-resolution, High S/N Spectroscopy

We obtained high-resolution, high S/N spectra for both stars using the High Resolution Echelle Spectrometer (HIRES; Vogt et al. 1994) on the Keck-I telescope in Hawaii. For HAT-P-32, we gathered 28 spectra with the I_2 absorption cell (Marcy & Butler 1992) between 2007 August and 2010 December, together with a single I_2-free template spectrum. We rejected one low S/N spectrum for which we were unable to obtain a high-precision RV measurement, and exclude from the analysis two spectra which were obtained during transit and thus may be affected by the Rossiter–McLaughlin effect (e.g., Queloz et al. 2000). For HAT-P-33, we gathered 22 spectra with the I_2 cell between 2008 September and 2010 December, and two template spectra. The HIRES spectra were reduced to barycentric RVs following Butler et al. (1996). The resulting measurements are given in Tables 3 and 4 for HAT-P-32 and HAT-P-33, respectively. The phased data, along with our best-fit models for both circular and eccentric orbits, are displayed in Figures 2 and 3.

For both candidates, the RV residuals from the best-fit model show significant scatter greatly in excess of what is expected based on the measurement uncertainties. For HAT-P-32, the residual rms is 80.3 m s^{-1} or 75.0 m s^{-1} for circular and eccentric models, respectively, while the rms expected from instrumental variations plus photon noise is only 15.7 m s^{-1}. For HAT-P-33, the residual rms is 55.7 m s^{-1} or 54.1 m s^{-1}, again for circular and eccentric models, respectively, while the expected rms is 7.9 m s^{-1}. Because of this high "jitter," we gathered substantially more high S/N spectra for these targets than we do for typical HATNet candidates. The reason for this is twofold: the high jitter could have been due to additional Keplerian motion due to the presence of additional planets in the systems which would be revealed by further observations, and in the presence of high jitter more observations are needed

Table 3
Relative Radial Velocities, Bisector Spans, and Activity Index Measurements of HAT-P-32

BJD[a] (2,454,000+)	RV[b] ($m\,s^{-1}$)	σ_{RV}[c] ($m\,s^{-1}$)	BS ($m\,s^{-1}$)	σ_{BS} ($m\,s^{-1}$)	S[d]	Phase
336.95660	−12.33	13.77	−4.23	22.35	0.240	0.168
337.12852	−51.77	12.83	−35.38	13.61	0.238	0.248
337.93027	...	...	8.77	12.61	0.233	0.621
337.93908	91.89	13.58	22.03	15.06	0.232	0.625
339.12681	−32.01	12.59	−5.23	17.10	0.239	0.177
339.92225	60.33	13.50	31.99	9.65	0.239	0.547
344.05490	−56.05	12.94	−7.56	12.17	0.232	0.469
345.14032[e]	−7.96	12.44	56.66	19.42	0.235	0.974
397.81437	−75.23	14.22	−36.38	9.63	0.236	0.474
398.09647	35.38	14.70	−41.76	8.10	0.234	0.605
427.84636	55.80	14.45	−55.48	12.13	0.235	0.442
428.85791	312.16	15.38	−57.89	15.15	0.240	0.912
429.92102	−3.17	14.43	−29.84	8.73	0.233	0.407
455.90267	−11.30	14.42	−35.44	17.49	0.231	0.491
458.93801	144.46	16.08	−9.85	11.93	0.232	0.903
460.86208	103.67	18.28	−9.84	11.05	0.230	0.798
548.72493	88.38	16.21	−19.13	14.89	0.240	0.664
635.11482	73.67	16.94	155.85	24.14	0.236	0.845
636.11275	−187.30	17.27	100.10	16.18	0.235	0.310
724.02617	−170.37	15.27	7.97	13.53	0.237	0.199
725.07143	37.66	16.62	89.82	14.96	0.241	0.686
727.11674	40.79	16.16	90.24	15.73	0.241	0.637
777.92375	−153.16	15.28	−28.12	10.06	0.232	0.268
810.82619	150.64	17.27	−20.45	12.98	0.230	0.571
838.93902	46.30	19.26	−33.20	13.87	0.225	0.647
1192.92153	−143.71	19.01	−28.23	13.83	0.236	0.289
1250.81416	−211.65	17.65	−30.15	10.29	0.238	0.216
1376.10348	−80.92	17.65	6.54	11.60	0.241	0.490
1544.91306[e]	−186.72	18.93	−81.83	21.62	0.224	0.006

Notes. For the iodine-free template exposures we do not measure the RV but do measure the BS and index S. Such template exposures can be distinguished by the missing RV value.
[a] Barycentric Julian dates throughout the paper are calculated from Coordinated Universal Time (UTC).
[b] The zero point of these velocities is arbitrary. An overall offset γ_{rel} fitted to these velocities in Section 3.4 has *not* been subtracted.
[c] Internal errors excluding the component of astrophysical jitter considered in Section 3.4.
[d] Chromospheric activity index calibrated to the scale of Vaughan et al. (1978) following Isaacson & Fischer (2010).
[e] Observation during transit which was excluded from the analysis.

Table 4
Relative Radial Velocities, Bisector Spans, and Activity Index Measurements of HAT-P-33

BJD[a] (2,454,000+)	RV[b] ($m\,s^{-1}$)	σ_{RV}[c] ($m\,s^{-1}$)	BS ($m\,s^{-1}$)	σ_{BS} ($m\,s^{-1}$)	S[d]	Phase
728.11380	...	...	−60.23	2.93	0.171	0.822
728.12071	107.70	6.84	−56.67	4.32	0.172	0.824
778.03749	−88.19	6.47	−59.99	4.67	0.174	0.190
779.11168	39.67	7.79	−16.02	6.12	0.173	0.499
780.05973	106.79	7.40	−2.11	4.05	0.173	0.772
791.11863	76.24	7.97	−4.56	4.00	0.174	0.955
805.96712	−168.48	7.63	83.04	6.79	0.171	0.229
807.00978	−76.74	9.16	74.87	7.06	0.170	0.529
807.99835	125.68	6.92	0.18	3.79	0.172	0.813
809.98993	13.78	9.01	−69.27	5.86	0.170	0.387
810.88079	125.60	8.34	−31.31	4.57	0.172	0.643
838.95648	41.95	7.70	5.62	5.71	0.172	0.724
865.01789	−25.12	8.25	16.88	4.31	0.171	0.224
954.83936	−67.35	7.49	7.29	4.92	0.175	0.076
955.85129	−52.75	8.95	−4.96	7.02	0.173	0.367
1192.01643	...	...	13.37	2.83	0.172	0.339
1192.02324	−93.30	7.19	22.62	3.46	0.173	0.341
1193.09374	−24.35	7.52	60.32	5.56	0.175	0.649
1193.93089	−8.61	8.57	38.64	5.33	0.170	0.890
1251.91465	13.52	7.72	16.56	4.23	0.172	0.578
1468.06245	22.33	7.86	91.25	6.82	0.173	0.789
1470.09079	18.65	8.16	−127.71	8.71	0.174	0.372
1545.09930	26.89	8.37	−5.60	5.38	0.170	0.961
1545.93211	−31.18	7.91	7.80	4.89	0.165	0.201

Notes. For the iodine-free template exposures we do not measure the RV but do measure the BS and index S. Such template exposures can be distinguished by the missing RV value.
[a] Barycentric Julian dates throughout the paper are calculated from Coordinated Universal Time (UTC).
[b] The zero point of these velocities is arbitrary. An overall offset γ_{rel} fitted to these velocities in Section 3.4 has *not* been subtracted.
[c] Internal errors excluding the component of astrophysical jitter considered in Section 3.4.
[d] Chromospheric activity index calibrated to the scale of Vaughan et al. (1978) following Isaacson & Fischer (2010).

to precisely determine the orbital parameters of the system. We consider further the origin of the jitter for each object in Section 3.2, concluding that it is most likely not due to additional planets, but rather due to stellar activity.

For each spectrum, we also calculated the spectral line bisector span (BS) following the method described in Section 5 of Bakos et al. (2007) and the activity index S calibrated to the scale of Vaughan et al. (1978) following the procedure of Isaacson & Fischer (2010). Note that for the BS we follow the convention BS $= v_1 - v_2$, where v_1 is the velocity of a point on the bisector near the continuum level and v_2 is the velocity of a point on the bisector near the line core. The BS and S values are plotted in Figures 2 and 3. For both stars, the BS and S values do not phase with the photometric ephemeris; however the scatters in the BS values are comparable to the RV semiamplitudes, so we are not able to rule out blend scenarios for either object based on the bisectors. Instead we rely on detailed blend modeling of the observations to rule out these scenarios as described in Section 3.3. For HAT-P-33, we found that the RV residuals are correlated with the BS (see also Section 3.2), and were thus able to use the BS to correct the RVs, reducing the effective jitter to $\sim 35\,m\,s^{-1}$.

2.4. Photometric Follow-up Observations

We conducted high-precision photometric observations of HAT-P-32 and HAT-P-33 using the KeplerCam CCD camera on the FLWO 1.2 m telescope. The observations for each target are summarized in Table 1. For HAT-P-32, in addition to observations taken during transit, we also obtained three sets of observations taken out of transit at the predicted times of secondary eclipse (assuming a circular orbit). These data are excluded from the global analysis described in Section 3.4, but are used in Section 3.3 in ruling out blend scenarios.

The reduction of the KeplerCam images was performed as described by Bakos et al. (2010). We performed External Parameter Decorrelation (EPD) and used the Trend Filtering Algorithm (TFA; Kovács et al. 2005) to remove trends simultaneously with the light curve modeling (for more details, see Bakos et al. 2010). The final time series, together with our best-fit transit light curve models, are shown in Figure 4; the individual

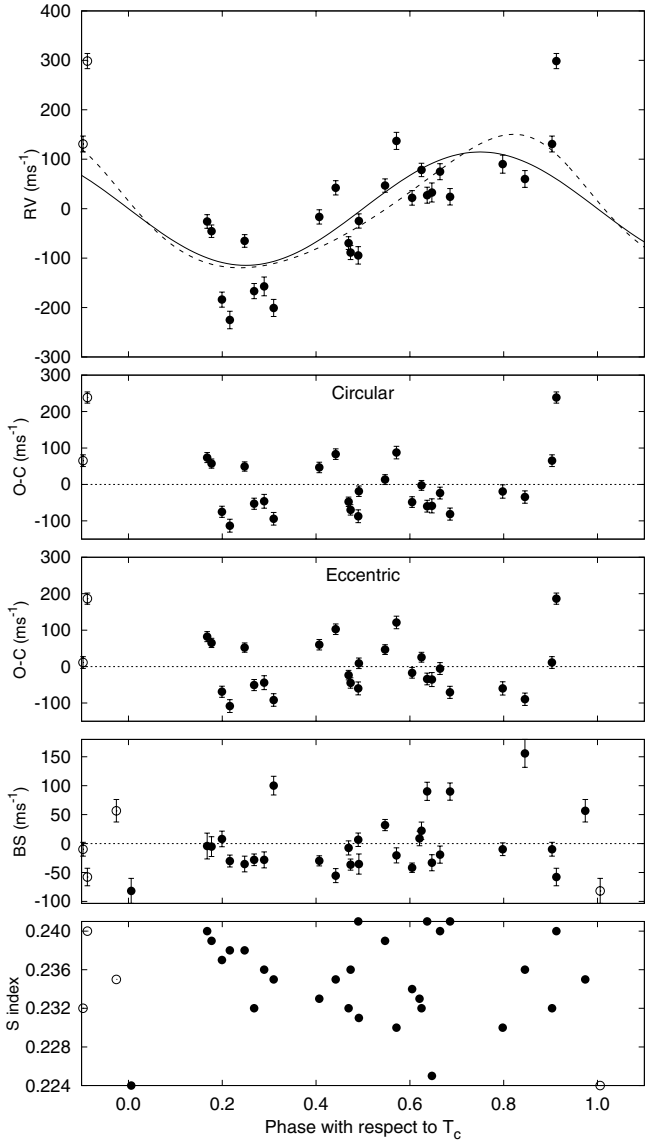

Figure 2. Top panel: Keck/HIRES RV measurements for HAT-P-32 shown as a function of orbital phase, along with our best-fit circular (solid line) and eccentric (dashed line) models as determined from our global modeling procedure (Section 3.4); see Table 8. Zero phase corresponds to the time of mid-transit. The center-of-mass velocity has been subtracted. Second panel: velocity $O-C$ residuals from the best-fit circular orbit. Jitter is not included in the error bars. Third panel: velocity $O-C$ residuals from the best-fit eccentric orbit. Fourth panel: bisector spans (BSs), with the mean value subtracted. The measurement from the template spectrum is included (see Section 3.3). Bottom panel: chromospheric activity index S measured from the Keck spectra. Note the different vertical scales of the panels. Observations shown twice are represented with open symbols.

measurements are reported in Tables 5 and 6 for HAT-P-32 and HAT-P-33, respectively.

3. ANALYSIS

3.1. Properties of the Parent Stars

Planetary parameters, such as the mass and radius, depend strongly on the stellar mass and radius, which in turn are constrained by the observed stellar spectra as well as the light curves and RV curves. We followed an iterative procedure, described by Bakos et al. (2010), to determine the relevant stellar parameters. The procedure involves iterating between

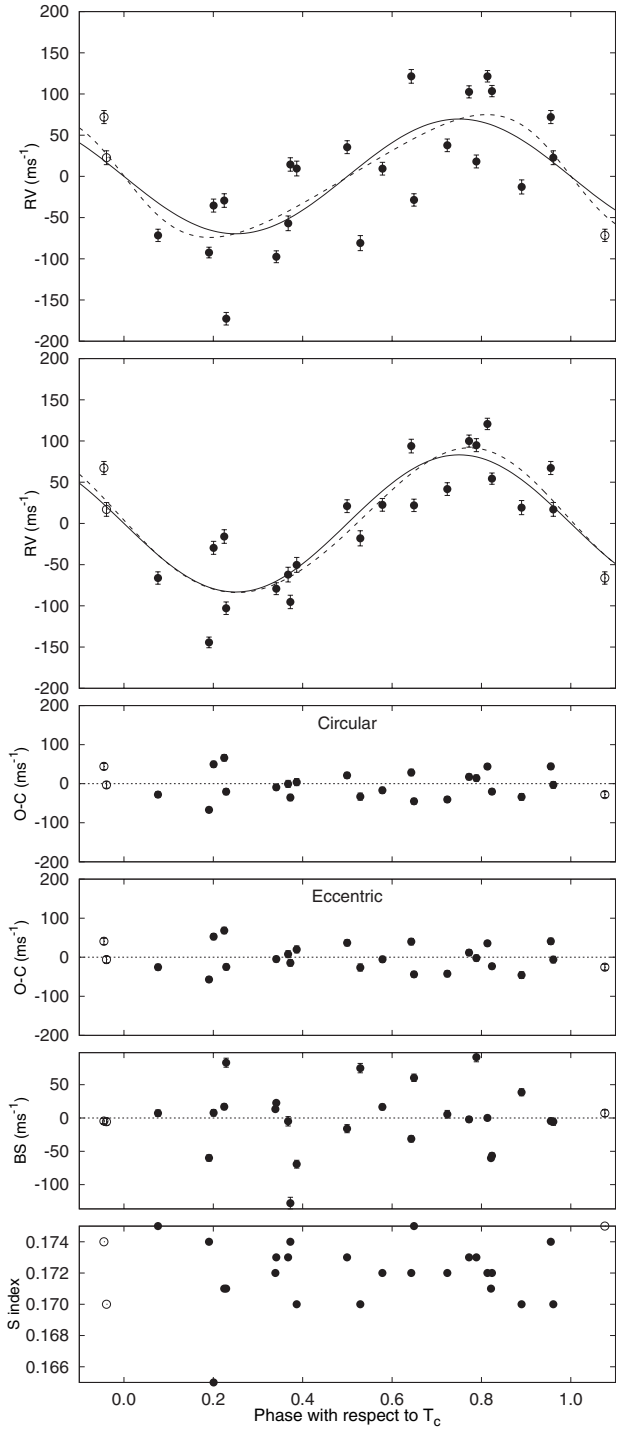

Figure 3. Top panel: Keck/HIRES RV measurements for HAT-P-33 shown as a function of orbital phase, along with our best-fit circular (solid line) and eccentric (dashed line) models as determined from our global modeling procedure (Section 3.4); see Table 9. Zero phase corresponds to the time of mid-transit. The center-of-mass velocity has been subtracted. Second panel: same as top panel—here we have subtracted a linear correlation with the spectral line bisector spans (BSs) from the RV measurements. This correlation was determined simultaneously with the fit, and significantly reduces the residual rms. For the displayed points, we subtract the correlation determined in the circular orbit fit. Third panel: velocity $O-C$ residuals from the best-fit circular orbit including the BS correlation. Jitter is not included in the error bars. Fourth panel: velocity $O-C$ residuals from the best-fit eccentric orbit including the BS correlation. Fifth panel: BS, with the mean value subtracted. The measurement from the template spectrum is included (see Section 3.3). Bottom panel: chromospheric activity index S measured from the Keck spectra. Note the different vertical scales of the panels. Observations shown twice are represented with open symbols.

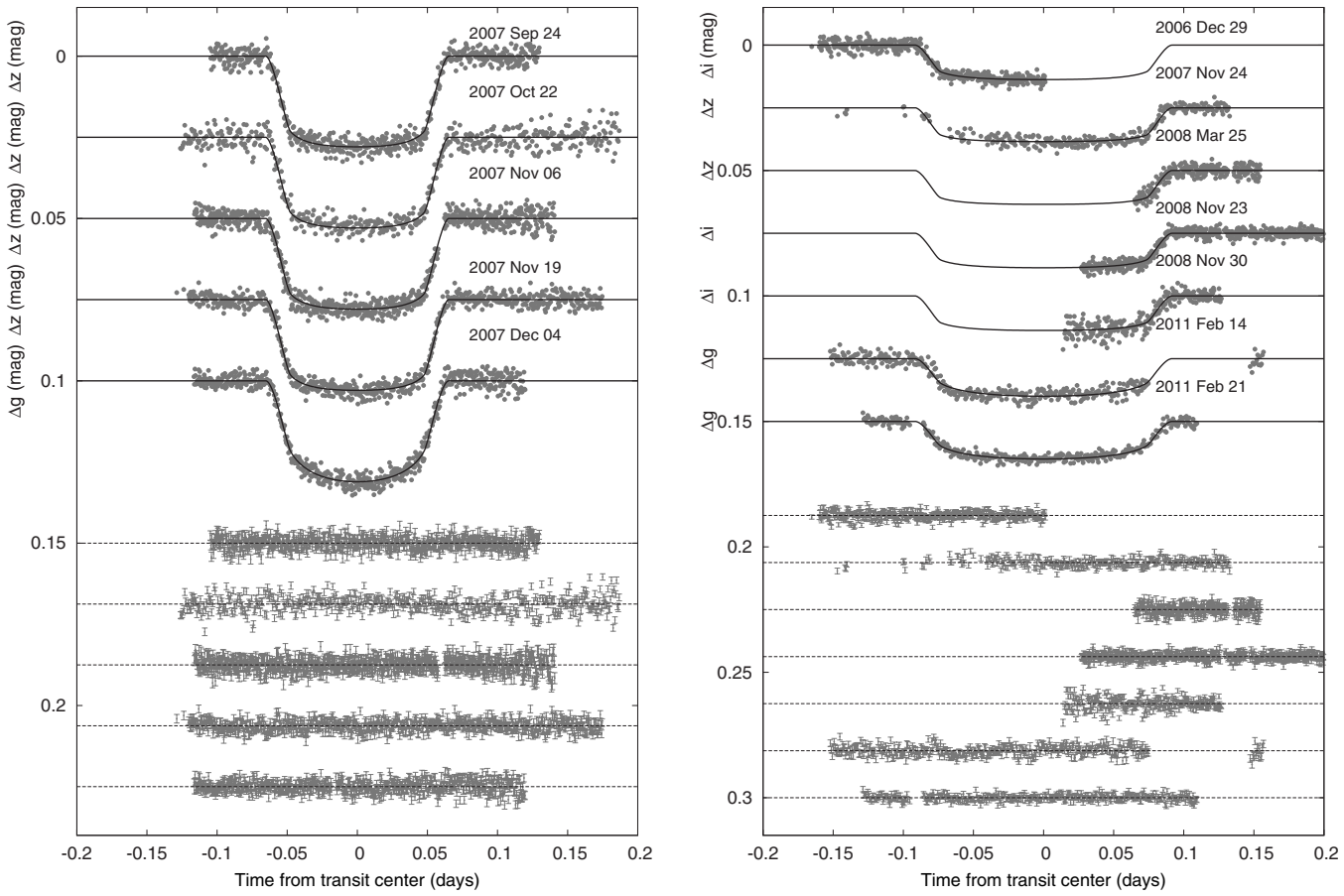

Figure 4. Unbinned transit light curves for HAT-P-32 (left) and HAT-P-33 (right), acquired with KeplerCam at the FLWO 1.2 m telescope. The light curves have been EPD and TFA processed, as described in Bakos et al. (2010). The dates of the events are indicated. The filters used are listed along the vertical axis. Curves after the first are displaced vertically for clarity. Our best fits from the global modeling described in Section 3.4 are shown by the solid lines. Residuals from the fits are displayed at the bottom, in the same order as the top curves. The error bars represent the photon and background shot noise, plus the readout noise.

Table 5
High-precision Differential Photometry of HAT-P-32

BJD (2,400,000 +)	Mag[a]	$\sigma_{\rm Mag}$	Mag(orig)[b]	Filter
54368.74140	−0.00204	0.00143	10.54500	z
54368.74180	0.00090	0.00144	10.54840	z
54368.74217	0.00417	0.00143	10.55120	z
54368.74255	−0.00158	0.00143	10.54590	z
54368.74296	0.00016	0.00142	10.54740	z
54368.74335	0.00079	0.00143	10.54810	z
54368.74373	0.00331	0.00144	10.55080	z
54368.74411	0.00071	0.00142	10.54810	z
54368.74449	−0.00132	0.00142	10.54610	z
54368.74489	−0.00129	0.00141	10.54610	z

Notes.
[a] The out-of-transit level has been subtracted. These magnitudes have been subjected to the EPD and TFA procedures, carried out simultaneously with the transit fit.
[b] Raw magnitude values without application of the EPD and TFA procedures.

(This table is available in its entirety in a machine-readable form in the online journal. A portion is shown here for guidance regarding its form and content.)

Table 6
High-precision Differential Photometry of HAT-P-33

BJD (2,400,000 +)	Mag[a]	$\sigma_{\rm Mag}$	Mag(orig)[b]	Filter
54099.68885	0.00058	0.00085	9.51222	i
54099.69425	0.00071	0.00083	9.51224	i
54099.69465	−0.00123	0.00083	9.51016	i
54099.69502	−0.00319	0.00083	9.50882	i
54099.69541	0.00122	0.00083	9.51279	i
54099.69579	0.00204	0.00083	9.51399	i
54099.69619	0.00045	0.00083	9.51219	i
54099.69659	−0.00038	0.00083	9.51120	i
54099.69697	−0.00305	0.00083	9.50858	i
54099.69735	−0.00342	0.00083	9.50826	i

Notes.
[a] The out-of-transit level has been subtracted. These magnitudes have been subjected to the EPD and TFA procedures, carried out simultaneously with the transit fit.
[b] Raw magnitude values without application of the EPD and TFA procedures.

(This table is available in its entirety in a machine-readable form in the online journal. A portion is shown here for guidance regarding its form and content.)

inferring stellar atmospheric parameters (including the effective temperature $T_{\rm eff\star}$, surface gravity $\log g_\star$, metallicity [Fe/H], and the projected rotation velocity $v \sin i$) from the Keck/HIRES template spectrum using the Spectroscopy Made Easy package (SME; Valenti & Piskunov 1996) and the Valenti & Fischer (2005) atomic line database, and modeling the light curves and RV curves (see Section 3.4) to determine the stellar density $\rho_\star$. At a given cycle in the iteration we combine our estimates

of $T_{\rm eff\star}$, [Fe/H], and $\rho_\star$ with the Yonsei–Yale (YY; Yi et al. 2001) series of stellar evolution models to determine the stellar mass, radius, and surface gravity among other parameters. If the resulting surface gravity differs significantly from the value determined from the spectrum with SME, we repeat the analysis fixing the surface gravity in SME to the new value.

For each star, the *initial* SME analysis, in which the surface gravity was allowed to vary, yielded the following values and uncertainties.

1. *HAT-P-32*: $T_{\rm eff\star} = 6001 \pm 88$ K, [Fe/H] $= -0.16 \pm 0.08$ dex, $\log g_\star = 4.02 \pm 0.07$ (cgs), and $v \sin i = 21 \pm 0.5\,{\rm km\,s^{-1}}$.
2. *HAT-P-33*: $T_{\rm eff\star} = 6234 \pm 114$ K, [Fe/H] $= -0.04 \pm 0.08$ dex, $\log g_\star = 3.86 \pm 0.10$ (cgs), and $v \sin i = 13.9 \pm 0.5\,{\rm km\,s^{-1}}$.

As described in Section 3.4 the inferred stellar densities, and hence radii, for HAT-P-32 and HAT-P-33 depend strongly on the orbital eccentricities, which due to the high RV jitters are poorly constrained. For each system we conducted separate analyses, first assuming a circular orbit and then allowing the eccentricity to vary. In each case we obtained a new value of $\log g_\star$ which we held fixed during a second SME iteration. The final stellar parameters for each star, assuming both circular and eccentric models, are listed in Table 7. As discussed in Section 3.4, for each system the assumed circular orbit model is preferred as the simplest model capable of fitting the data. We therefore provisionally suggest adopting the circular orbit models for applications which require a single set of parameters for each system; however we note that this may underestimate the true parameter uncertainties.

The inferred location of each star for both the circular and eccentric models, in diagrams of $a/R_\star$ (which is related to $\rho_\star$; e.g., see Seager & Mallén-Ornelas 2003) versus $T_{\rm eff\star}$, analogous to the classical H-R diagram, is shown in Figures 5 and 6. In each case the stellar properties and their 1σ and 2σ confidence ellipsoids are displayed against the backdrop of model isochrones for a range of ages and the appropriate stellar metallicity.

As a check on our stellar parameter determinations we compare the measured photometric colors of the two stars to the predicted values based on the models. HAT-P-32 has $J - K = 0.281 \pm 0.008$[11] and $V - I_C = 0.62 \pm 0.10$ (from two-armed spiral shock (TASS); Droege et al. 2006), whereas the predicted values are $J - K = 0.32 \pm 0.02$ and $V - I_C = 0.574 \pm 0.023$ for the circular model, and $J - K = 0.34 \pm 0.02$ and $V - I_C = 0.592 \pm 0.024$ for the eccentric model. In both cases the model $V - I_C$ colors are consistent with the measurements, but the model $J-K$ colors are slightly ($\sim 2\sigma$) redder than the measurements. HAT-P-33 has $J - K = 0.280 \pm 0.030$ and $V - I_C = 0.577 \pm 0.087$ (also from 2MASS and TASS), and has predicted values of $J - K = 0.27 \pm 0.02$ and $V - I_C = 0.511 \pm 0.022$ for the circular model and $J - K = 0.28 \pm 0.02$ and $V - I_C = 0.522 \pm 0.022$ for the eccentric model. The measured photometric colors of HAT-P-33 are within 1σ of the predicted values for both models.

Neither HAT-P-32 nor HAT-P-33 shows significant chromospheric emission in their Ca II H and K line cores. Following the procedure of Isaacson & Fischer (2010), we find median $\log R'_{\rm HK}$ (Noyes et al. 1984) values of -4.62 and -4.88 for HAT-P-32 and HAT-P-33, respectively.

3.2. Stellar Jitter

Both HAT-P-32 and HAT-P-33 exhibit notably high scatter in their velocity residuals. Stellar jitter values of $78.7\,{\rm m\,s^{-1}}$ and $55.1\,{\rm m\,s^{-1}}$ for HAT-P-32 and HAT-P-33, respectively, must be added in quadrature to their velocity errors to achieve reduced χ^2 values of unity for the best-fit circular orbits (see Section 3.4).

A possible cause of the jitter is the presence of one or more additional planets in either system, though this would not explain the high scatter seen in the BS measurements. Figure 7 shows the Lomb–Scargle frequency spectra (L-S; Lomb 1976; Scargle 1982; Press & Rybicki 1989) of the RV observations for both stars computed up to a maximum frequency of $2.0\,{\rm d^{-1}}$. In both cases there is a peak in the spectrum at the transit frequency; in the case of HAT-P-32 this is the highest peak in the spectrum, while in the case of HAT-P-33 the highest peak is at a high-frequency alias of the transit frequency (if we restrict the search to frequencies shorter than $0.49\,{\rm d^{-1}}$, the transit frequency is the highest peak). We note that in neither case would the planet be detectable from the RV data alone. For HAT-P-32, the false-alarm probability of detecting a peak in the L-S periodogram with a height greater than or equal to the measured peak height is $\sim$8% (this is determined by applying L-S to simulated Gaussian white noise RV curves with the same time sampling as the observations). For HAT-P-33, the false-alarm probability of the transit peak is 79% (the false-alarm probability for the highest peak in the spectrum is 30%). We also show the L-S spectra of the RV residuals from the best-fit circular orbit models, in order to see if there is evidence for additional short-period planets in the systems. The highest peaks in these spectra are at periods of 18.104 d and 0.8507 d for HAT-P-32 and HAT-P-33, respectively. If we assume that each system has an additional planet at the periods stated above, the rms of the RV residuals decreases to $\sim 40\,{\rm m\,s^{-1}}$ and $\sim 30\,{\rm m\,s^{-1}}$ for HAT-P-32 and HAT-P-33, respectively. However, these peaks have corresponding false-alarm probabilities of 8% and 8.9%, so they are not statistically significant detections. We conclude that while either system may host additional short-period planets, there are not at present enough RV observations to make a statistically significant detection.

For each system there is some ambiguity in the peak that depends on the method used to scan for additional signals. As an alternative analysis we fit the RV observations of each system using a function of the form

$$\mathrm{RV_{obs}}(t) = \gamma + \dot{\gamma} t + \mathrm{RV_{orb}}(t) + A \sin 2\pi f t + B \cos 2\pi f t, \quad (1)$$

where $\dot{\gamma}$ is a constant acceleration (assumed to be zero for HAT-P-33), $\mathrm{RV_{orb}}(t)$ is an eccentric orbit with fixed period and epoch of transit, and A and B are free parameters. We scan through f optimizing all free parameters at each trial frequency. When scanning over the frequency range $0.001\,{\rm d^{-1}} < f < 2.49\,{\rm d^{-1}}$, we find $f = 0.0208\ {\rm d^{-1}}$ or $P = 47.962$ d for HAT-P-32 and $f = 2.178\,{\rm d^{-1}}$ or $P = 0.459$ d for HAT-P-33. If we limit the frequency scan to $f < 0.49\ {\rm d^{-1}}$, we find $f = 0.09545\ {\rm d^{-1}}$ or $P = 10.476$ d for HAT-P-33.

Another potential source of RV and BS jitter is varying scattered moonlight contaminating the spectra. Following Kovács et al. (2010), we investigated the possibility that the BS and RV may be affected by varying sky contamination, and found no

[11] Taken from Two Micron All Sky Survey (2MASS; Skrutskie et al. 2006) and converted to the ESO photometric system using the transformations by Carpenter (2001).

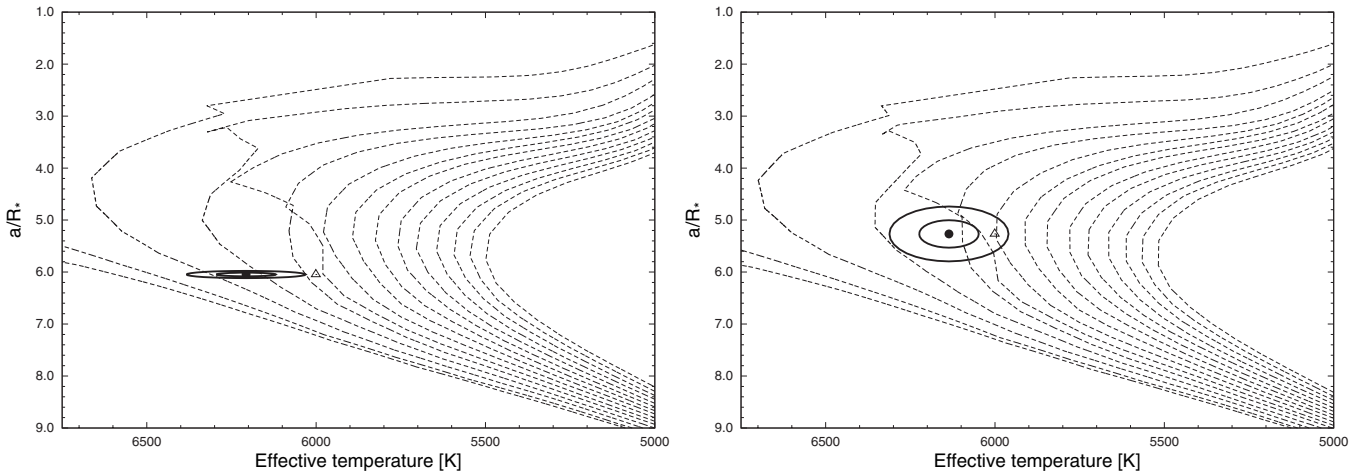

Figure 5. Model isochrones from Yi et al. (2001) assuming a circular orbit (left) and the best-fit eccentric orbit (right) for the measured metallicity of HAT-P-32, and ages of 0.5 Gyr and 1–14 Gyr in 1 Gyr steps (left to right in each plot). The adopted values of $T_{\rm eff\star}$ and $a/R_\star$ are shown together with their 1σ and 2σ confidence ellipsoids. The initial values of $T_{\rm eff\star}$ and $a/R_\star$ from the first SME and light curve analyses are represented with a triangle.

Table 7
Stellar Parameters for HAT-P-32 and HAT-P-33

Parameter	HAT-P-32		HAT-P-33		Source
	Value[a] Circular	Value Eccentric	Value[a] Circular	Value Eccentric	
Spectroscopic properties					
$T_{\rm eff\star}$ (K)	6207 ± 88	6001 ± 88	6446 ± 88	6401 ± 88	SME[b]
[Fe/H]	-0.04 ± 0.08	-0.16 ± 0.08	0.07 ± 0.08	0.05 ± 0.08	SME
$v \sin i$ (km s^{-1})	20.7 ± 0.5	21 ± 0.5	13.7 ± 0.5	13.8 ± 0.5	SME
$v_{\rm mac}$ (km s^{-1})	4.69	4.3	5.06	4.99	SME
$v_{\rm mic}$ (km s^{-1})	0.85	0.0	0.85	0.85	SME
$\gamma_{\rm RV}$ (km s^{-1})	-23.21 ± 0.26	...	23.03 ± 0.28	...	DS[c]
Photometric properties					
V (mag)	11.289	...	11.188	...	TASS
$V - I_C$ (mag)	0.62 ± 0.10	...	0.577 ± 0.087	...	TASS
J (mag)	10.251 ± 0.022	...	10.263 ± 0.021	...	2MASS
H (mag)	10.024 ± 0.022	...	10.061 ± 0.024	...	2MASS
K_s (mag)	9.990 ± 0.022	...	10.004 ± 0.018	...	2MASS
Derived properties					
$M_\star$ ($M_\odot$)	1.160 ± 0.041	$1.176^{+0.043}_{-0.070}$	1.375 ± 0.040	1.403 ± 0.096	YY+$a/R_\star$+SME[d]
$R_\star$ ($R_\odot$)	1.219 ± 0.016	1.387 ± 0.067	1.637 ± 0.034	1.777 ± 0.280	YY+$a/R_\star$+SME
$\log g_\star$ (cgs)	4.33 ± 0.01	4.22 ± 0.04	4.15 ± 0.01	4.09 ± 0.11	YY+$a/R_\star$+SME
$L_\star$ ($L_\odot$)	1.97 ± 0.15	2.43 ± 0.30	4.15 ± 0.33	$4.73^{+1.87}_{-1.25}$	YY+$a/R_\star$+SME
M_V (mag)	4.04 ± 0.10	3.82 ± 0.14	3.19 ± 0.10	3.06 ± 0.35	YY+$a/R_\star$+SME
M_K (mag, ESO)	2.77 ± 0.04	2.50 ± 0.11	2.11 ± 0.05	1.93 ± 0.34	YY+$a/R_\star$+SME
Age (Gyr)	2.7 ± 0.8	$3.8^{+1.5}_{-0.5}$	2.3 ± 0.3	2.4 ± 0.4	YY+$a/R_\star$+SME
Distance (pc)	283 ± 5	320 ± 16	387 ± 9	419 ± 66	YY+$a/R_\star$+SME

Notes.

[a] The eccentricities of both HAT-P-32 and HAT-P-33 are poorly constrained—both planets are consistent with circular orbits but may also have significant eccentricities. We list separately the parameters obtained when a circular orbit is fixed, and when the eccentricity is allowed to vary. As shown in Section 3.4, for each system the circular orbit model is preferred as the simplest model capable of fitting the observations (the Bayesian Information Criterion is lower for the circular models than the eccentric ones). For applications requiring a single set of parameters for each system we thus provisionally suggest adopting the circular orbit parameters; however we note that in this case the parameter uncertainties may be underestimated.

[b] SME = "Spectroscopy Made Easy" package for the analysis of high-resolution spectra (Valenti & Piskunov 1996). These parameters rely primarily on SME, but have a small dependence also on the iterative analysis incorporating the isochrone search and global modeling of the data, as described in the text.

[c] The mean heliocentric velocity as measured by the CfA Digital Speedometer. The uncertainty is the rms of the measured velocities of the star rather than the uncertainty on the mean.

[d] YY+$a/R_\star$+SME = based on the YY isochrones (Yi et al. 2001), $a/R_\star$ as a luminosity indicator, and the SME results.

evidence that this is the case. Alternatively, RV and BS jitter might be caused by variable contamination from a nearby star. Based on our KeplerCam observations of HAT-P-32 and HAT-P-33, we can rule out contaminating neighbors with $\Delta i \lesssim 5$ mag at a separation greater than $3''$, or neighbors with $\Delta i \lesssim 2$ mag at a separation greater than $1''$ of either star. We cannot rule out fainter close neighbors which could be responsible for at least some of the jitter. Constraints on potential neighbors based on

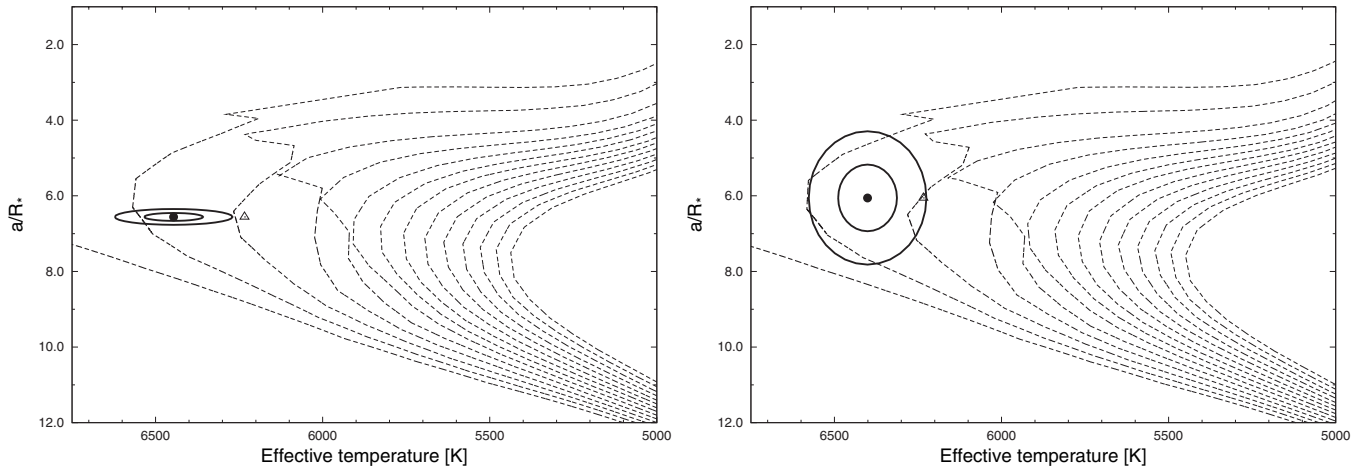

Figure 6. Same as Figure 5—here we show the results for HAT-P-33. In this case the 0.5 Gyr isochrone is not included.

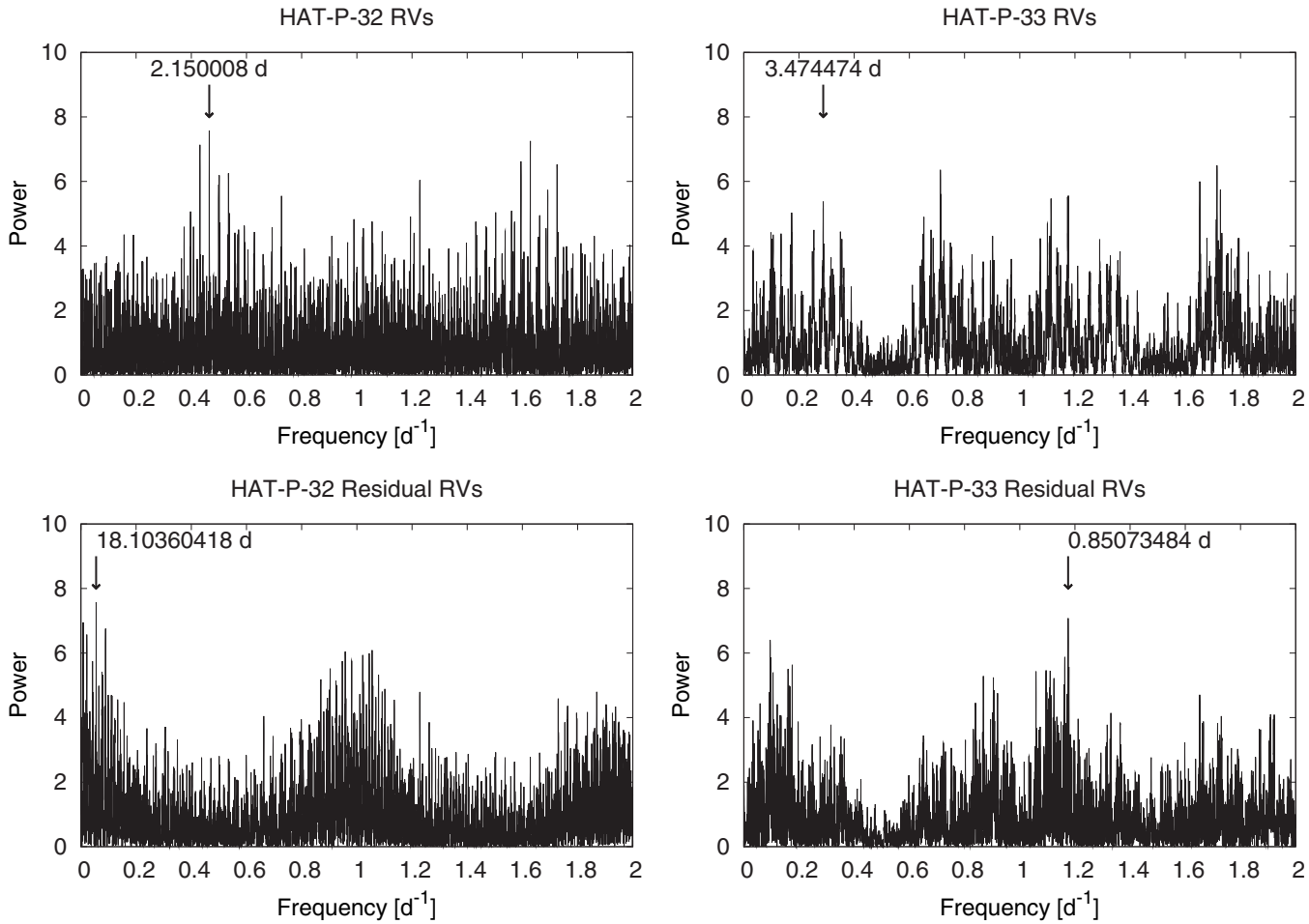

Figure 7. Lomb–Scargle frequency spectra for the RVs (top) and residual RVs from the best-fit circular orbit models (bottom) for HAT-P-32 (left) and HAT-P-33 (right). In the top panels we mark the transit frequencies, while in the bottom panels we mark the highest peaks in the spectra. In all cases the false-alarm probability of finding a peak as high as the marked peak in a Gaussian white noise RV curve is greater than 8%.

modeling the photometric light curves are further considered in Section 3.3.

Figure 8 compares the RV residuals to the BSs for HAT-P-32 and HAT-P-33. For HAT-P-33, there is a clear anti-correlation between these quantities (the Spearman rank-order correlation test (e.g., Press et al. 1992) yields a correlation coefficient of $r_s = -0.77$ with a false-alarm probability of 0.04% assuming a circular orbit, while for the best-fit eccentric orbit $r_s = -0.72$ with a 0.1% false-alarm probability). For HAT-P-32, there is a hint of an anti-correlation, but it is not statistically significant ($r_s = -0.30$ with a false-alarm probability of 14% assuming a circular orbit, and $r_s = -0.39$ with 4.9% false-alarm probability for the best-fit eccentric orbit). The anti-correlation for HAT-P-33 is an indication that the measured jitter for this star is dominated by intrinsic stellar variations, rather than being due to another planet in the system, or to the instrumental errors being

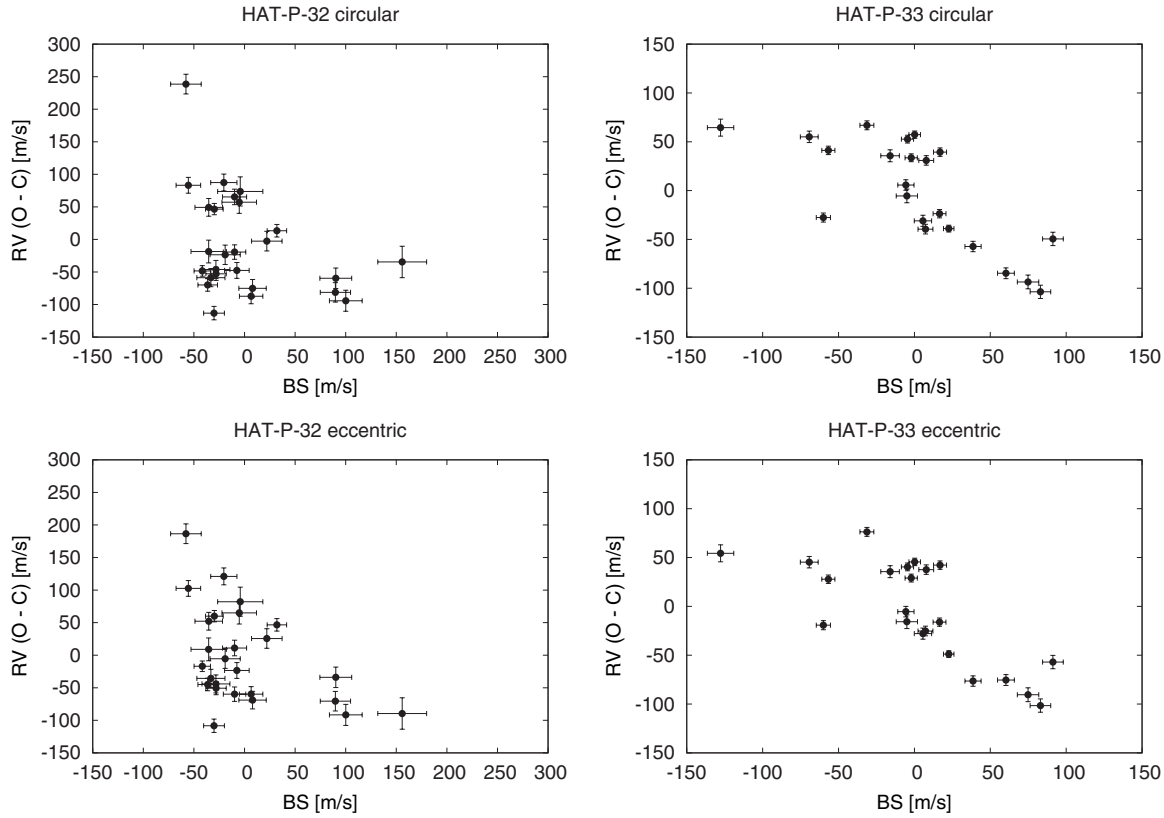

Figure 8. RV residuals from the best-fit circular (top) and eccentric (bottom) model orbits vs. BS for HAT-P-32 (left) and HAT-P-33 (right). There is a hint of an anti-correlation between these quantities for HAT-P-32, though it is not statistically significant. For HAT-P-33 the quantities are clearly anti-correlated. See the discussion in Section 3.2.

underestimated. We make use of this correlation in Section 3.4 to reduce the scatter in the RV residuals for HAT-P-33 and to improve the precision of the fitted parameters. We note that other investigators have previously made use of correlations between RV residuals and BS measurements to improve the precision of RV measurements (e.g., Melo et al. 2007).

Saar et al. (1998) argue that the RV jitter of F stars is due primarily to convective inhomogeneities (due, for example, to regions of strong magnetic fields which locally suppress convection) which vary in time, rather than temperature inhomogeneities (due, for example, to cool star spots) which vary in time. The latter may be more important for G and K stars. Both sources of jitter would result in significant BS variations that may be correlated with the RV variations, but the lack of detectable out-of-transit photometric variations in the HATNet light curves of HAT-P-32 and HAT-P-33, and the fact that neither star shows particularly high chromospheric emission in its Ca II H and K line cores, is consistent with the expectation that temporally changing convective inhomogeneities, rather than temporally changing temperature inhomogeneities, are responsible for the jitter of these two stars.

Jitter values as high as those found for HAT-P-32 and HAT-P-33 are typical of stars with similar spectral types and rotation velocities. From the $v \sin i$–jitter correlation measured by Saar et al. (2003), the expected jitter for an F dwarf with $v \sin i = 20\,\mathrm{km\,s^{-1}}$ is $\sim$50 m s^{-1}, while for an F dwarf with $v \sin i = 14\,\mathrm{km\,s^{-1}}$ the expected jitter is $\sim$30 m s^{-1}. The sample used by Saar et al. (2003) to determine this correlation includes only a handful of stars with $v \sin i > 10\,\mathrm{km\,s^{-1}}$, and the scatter about the relation is fairly significant—one star with $v \sin i \sim 15\,\mathrm{km\,s^{-1}}$ was found to have a jitter in excess of 100 m s^{-1}. The planet-hosting star HAT-P-2, which has a similar temperature and rotation velocity to HAT-P-32 and HAT-P-33 ($T_{\mathrm{eff}\star} = 6290 \pm 60$ K, $v \sin i = 20.8 \pm 0.3\,\mathrm{km\,s^{-1}}$; Pál et al. 2010), has been reported to have a high jitter of $\sim$60 m s^{-1} based on data from Keck and Lick (Bakos et al. 2007). A subsequent analysis by Winn et al. (2007), using only Keck/HIRES data, found a somewhat lower jitter of $\sim$30 m s^{-1}, though this is still quite a bit higher than most planet-hosting stars discovered to date (e.g., the median jitter of the previously published HATNet planets is $\sim$7 m s^{-1}). The primary difference between HAT-P-2 and the two systems presented here is that the planet HAT-P-2b is significantly more massive than either HAT-P-32b or HAT-P-33b (HAT-P-2b has $M_p = 9.09 \pm 0.24\,M_{\mathrm{J}}$; Pál et al. 2010); as a result, the RV semiamplitude of HAT-P-2b ($K = 984 \pm 17\,\mathrm{m\,s^{-1}}$) greatly exceeds the jitter, making this planet more straightforward to confirm than either HAT-P-32b or HAT-P-33b.

3.3. Excluding Blend Scenarios

Both HAT-P-32 and HAT-P-33 exhibit significant spectral line BS variations (Figures 2 and 3; the rms of the BS is 53 m s^{-1} and 51 m s^{-1} for HAT-P-32 and HAT-P-33, respectively). In neither case are the variations in phase with the transit ephemeris, as one might expect if the observed RV variation were due to a blend between an eclipsing binary system and another star. As discussed in Section 3.2, these variations are likely due to temporally changing convective inhomogeneities, perhaps created by variable photospheric magnetic faculae as in the Sun, which we suspect are responsible for the significant RV jitter seen in both of these stars. Nonetheless the large BS variations, which are comparable to the semiamplitudes of the RV signals,

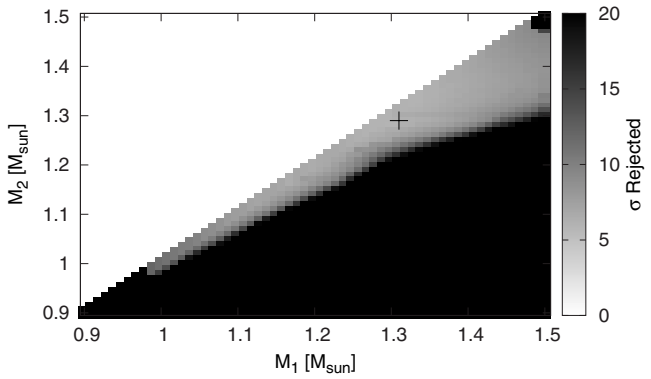

Figure 9. σ-level at which the class 3 blend model (hierarchical triple stellar system) can be rejected for HAT-P-33 as a function of the masses of the two largest stars in the system: M_1 is the mass of the uneclipsed star, and M_2 is the mass of the primary star in the eclipsing system. Note that the lack of several km s^{-1} RV variations leads to the constraint $M_1 > M_2$. The best-fit model, indicated on the plot with a cross, is rejected with $\sim 6\sigma$ confidence.

prevent us from using the BSs to rule out the possibility that either of these systems is a blend.

To rule out blend scenarios we made use of the BLENDANAL program (Hartman et al. 2011b; see also Hartman et al. 2011a) which models the observed light curves, stellar atmospheric parameters, and calibrated photometric magnitudes using various blended eclipsing binary scenarios as well as scenarios involving a transiting planet system potentially blended with light from another star. The program relies on a combination of the Padova (Girardi et al. 2000) and Baraffe et al. (1998) stellar evolution models, the Eclipsing Binary Orbit Program (EPOP; Popper & Etzel 1981; Etzel 1981; Nelson & Davis 1972) as modified by Southworth et al. (2004a, 2004b), and stellar limb-darkening parameters from Claret (2004). It is similar to the BLENDER program (Torres et al. 2005) which has been used to confirm *Kepler* planets (e.g., Torres et al. 2011), but with a number of technical differences which are described by Hartman et al. (2011b).

For each object we fit four classes of models.

1. A single star with a transiting planet.
2. A planet transiting one component of a binary star system.
3. A hierarchical triple stellar system.
4. A blend between a bright stationary star and a fainter, physically unrelated eclipsing binary.

Initially, we assume that the eclipsing components have a circular orbit. For both HAT-P-32 and HAT-P-33, we find that the class 1 model (a single star with a transiting planet) or the class 2 model with a planet-hosting star that is much brighter than its binary star companion provide better fits (lower χ^2) than the class 3 and class 4 models. To evaluate the statistical significance with which the class 3 and class 4 models may be rejected, we follow the Monte Carlo procedure described in Hartman et al. (2011a). We find that for HAT-P-32 we may reject both the class 3 and 4 models with $\sim 13\sigma$ confidence (the best-fit class 4 model consists of a group of stars with similar parameters to the best-fit class 3 model), while for HAT-P-33 we may reject the class 3 and 4 models with $\sim 6\sigma$ confidence (e.g., Figure 9).

For both HAT-P-32 and HAT-P-33, the eclipsing binary star blend scenarios (classes 3 and 4) are excluded in part due to the lack of an apparent secondary eclipse or out-of-transit variation that are predicted by models capable of fitting the observed primary transits. For HAT-P-33 the HATNet light curve provides these constraints, while for HAT-P-32 three sets of KeplerCam observations collected during predicted secondary eclipses (assuming a circular orbit) augment the constraints provided by the HATNet light curve. Figure 10 shows a few example model light curves for the best-fit class 4 model for HAT-P-32 which illustrate this.

Because the time of secondary eclipse depends on the eccentricity, which is poorly constrained by the RV observations, we repeat the blend analysis for both systems fixing the eccentricities to the best-fit values as determined in Section 3.4. While for HAT-P-32 this scenario causes the secondary eclipses to not occur during the out-of-transit KeplerCam observations, the eccentric eclipsing binary results in stronger out-of-transit variations which are ruled out by the HATNet data. In this case for HAT-P-32, we may reject the class 3 and 4 models with $>11\sigma$ confidence. For HAT-P-33, we may reject the class 3 and 4 models with $>7\sigma$ confidence.

For the class 2 models we consider two cases, one in which the transiting planet orbits the brighter binary star component, and the other in which the planet orbits the fainter binary star component. In both cases the spectroscopic temperature and the photometric colors constrain the brighter star to have a mass of $\gtrsim 1\,M_\odot$ for both systems. We find that the case of the planet orbiting the fainter component can be rejected outright with $>4\sigma$ confidence for both HAT-P-32 and HAT-P-33. The case of a planet orbiting the brighter binary star component amounts to including third light in the fit. When the secondary star contributes negligible light to the system, the model becomes indistinguishable from the best-fit case 1 model; such a model cannot be ruled out with the available data. Instead we may place an upper limit on the mass of any binary star companion. For HAT-P-32 we find that a putative companion must have $M < 0.5\,M_\odot$ with 5σ confidence, while for HAT-P-33 a companion must have $M < 0.55\,M_\odot$ with 5σ confidence. These translate into upper limits on the secondary-to-primary V-band luminosity ratio of $\sim 1\%$ for both HAT-P-32 and HAT-P-33.

Based on the above discussion we conclude that the signals detected in the HAT-P-32 and HAT-P-33 light curves and RV curves are planetary in nature.

3.4. Global Modeling of the Data

We modeled the HATNet photometry, the follow-up photometry, and the high-precision RV measurements using the procedure described in detail by Pál et al. (2008) and Bakos et al. (2010). One significant difference from our previous planet discoveries is that we use a Mandel & Agol (2002) transit model to describe the HATNet photometry, rather than a simplified no-limb-darkening model. This was necessary due to the high S/N HATNet detections, especially for HAT-P-32. To describe the follow-up light curves, we use a Mandel & Agol (2002) transit model together with the simultaneous EPD and TFA model of instrumental variations (Bakos et al. 2010), and we use a Keplerian orbit to describe the RV curves. For HAT-P-33, we include a term $\alpha_{\rm BS} \times$ BS in the RV model, where $\alpha_{\rm BS}$ is a free parameter describing the residual RV–BS correlation, as we found that this significantly reduces the RV residuals. For HAT-P-32, we do not include this correction because the residual RV–BS correlation is not statistically significant. For each planetary system we fit two models, one in which the eccentricity is fixed to zero, and another in which the eccentricity varies. The parameters for each system are listed in Tables 8 and 9.

As described in Bakos et al. (2010), we use a combination of the downhill simplex method (e.g., Press et al. 1992) and the classical linear least-squares algorithm to initially

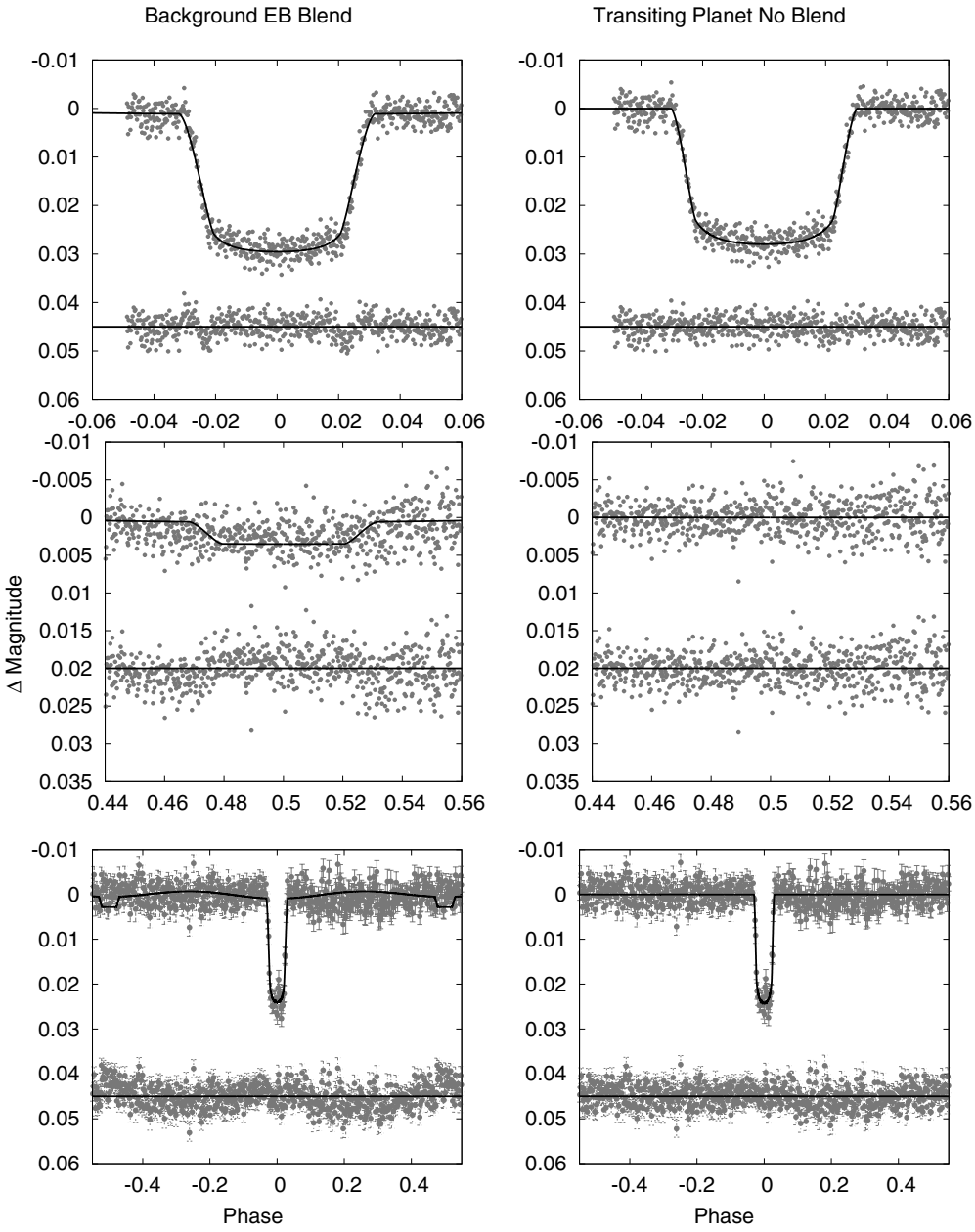

Figure 10. Comparison of the best-fit class 4 (background eclipsing binary; left) and class 1 (single star with a transiting planet; right) blend models for HAT-P-32. The results are shown for three illustrative light curves: a KeplerCam z-band primary transit from 2007 September 24 (top), a KeplerCam z-band out-of-transit light curve from 2007 December 3 (middle), and the I_C-band HATNet field G125 light curve (bottom). The HATNet light curve is folded and binned in phase, using a bin size of 0.002 ($\sim$6.2 minutes; note that the binning is only for display purposes—we do not bin the data in the modeling). In each panel the light curve is shown at top together with the model, and the residual is shown below. Note that for the KeplerCam observations we plot the EPD/TFA-corrected light curve; this correction is determined simultaneously with the fit and as a result there are slight differences in the plotted KeplerCam light curves for the two classes of blend models. The class 4 blend model provides a notably poorer fit to the light curves than the class 1 model—this includes slight differences in the ingress/egress of the primary transit, and a secondary transit and an out-of-transit variation which are not seen in the KeplerCam or HATNet data.

optimize the free parameters, and then use the Markov Chain Monte Carlo method (MCMC; Ford 2006) to determine the parameter uncertainties (we use the "Hyperplane-CLLS" variant described in Bakos et al. 2010). Here, we provide a few additional details not given in Bakos et al. (2010). For each system/model we generate a single chain of 20,000 links using the Metropolis–Hastings algorithm (e.g., Press et al. 2007). We start the chain from the optimized position, assuming a uniform prior distribution for each of the jump parameters (listed in Bakos et al. 2010), and drawing them from a Gaussian proposal distribution with eigenvalues and eigenvectors derived from the Fisher covariance matrix analytically evaluated at the optimal position. We inspected the resulting parameter chains to verify that with this procedure it is not necessary to include a "burn-in" phase.

Neither system has a clearly non-zero eccentricity. Using the Lucy & Sweeney (1971) test, we find that there is a non-negligible $\sim$3% probability that the eccentricity found for HAT-P-32 arises by chance from a circular orbit, while for HAT-P-33 the probability is $\sim$20%. As an alternative approach we calculate the Bayesian Information Criterion (BIC; Schwarz 1978; Liddle 2007) for the circular and eccentric models, taking

Table 8
Orbital and Planetary Parameters for HAT-P-32b

Parameter	Value[a] Circular	Value Eccentric
Light curve parameters		
P (days)	2.150008 ± 0.000001	2.150009 ± 0.000001
T_c (BJD)[b]	$2454420.44637 \pm 0.00009$	$2454416.14639 \pm 0.00009$
T_{14} (days)[b]	0.1295 ± 0.0003	0.1292 ± 0.0003
$T_{12} = T_{34}$ (days)[b]	0.0172 ± 0.0002	0.0171 ± 0.0002
$a/R_\star$	$6.05^{+0.03}_{-0.04}$	5.32 ± 0.22
$\zeta/R_\star$[c]	17.80 ± 0.03	17.84 ± 0.03
$R_p/R_\star$	0.1508 ± 0.0004	0.1508 ± 0.0004
b^2	$0.014^{+0.014}_{-0.008}$	$0.012^{+0.012}_{-0.007}$
$b \equiv a \cos i/R_\star$	$0.117^{+0.045}_{-0.047}$	$0.108^{+0.043}_{-0.044}$
i (deg)	88.9 ± 0.4	88.7 ± 0.6
Limb-darkening coefficients[d]		
c_1, i (linear term)	0.2045	0.2098
c_2, i (quadratic term)	0.3593	0.3562
c_1, z	0.1527	0.1580
c_2, z	0.3513	0.3476
c_1, g	0.4460	0.4564
c_2, g	0.3107	0.3027
RV parameters		
K (m s^{-1})	122.8 ± 23.2	136.1 ± 23.8
$e \cos(\omega)$[e]	0.000 ± 0.000	0.099 ± 0.080
$e \sin(\omega)$[e]	0.000 ± 0.000	0.124 ± 0.037
e	0.000 ± 0.000	0.163 ± 0.061
ω (deg)	0 ± 0	52 ± 29
RV jitter (m s^{-1})	78.7	73.3
Secondary eclipse parameters		
T_s (BJD)	2454421.521 ± 0.000	2454417.357 ± 0.109
$T_{s,14}$	0.1295 ± 0.0003	0.1653 ± 0.0120
$T_{s,12}$	0.0172 ± 0.0002	0.0221 ± 0.0017
Planetary parameters		
M_p (M_J)	0.860 ± 0.164	0.941 ± 0.166
R_p (R_J)	1.789 ± 0.025	2.037 ± 0.099
$C(M_p, R_p)$[f]	0.10	0.27
ρ_p (g cm^{-3})	0.19 ± 0.04	$0.14^{+0.03}_{-0.02}$
$\log g_p$ (cgs)	$2.82^{+0.07}_{-0.10}$	2.75 ± 0.07
a (AU)	0.0343 ± 0.0004	$0.0344^{+0.0004}_{-0.0007}$
$T_{\rm eq}$ (K)	1786 ± 26	1888 ± 51
Θ[g]	0.028 ± 0.005	0.027 ± 0.004
$\langle F \rangle$ (10^9 erg s^{-1} cm^{-2})[h]	2.29 ± 0.13	2.86 ± 0.31

Notes.
[a] The eccentricity of HAT-P-32 is poorly constrained. We list separately the parameters obtained when a circular orbit is fixed, and when the eccentricity is allowed to vary. As shown in Section 3.4, the circular orbit model is preferred as the simpler model capable of fitting the observations (the Bayesian Information Criterion is lower for the circular model than the eccentric one). For applications requiring a single set of parameters we thus provisionally suggest adopting the circular orbit parameters; however we note that in this case the parameter uncertainties may be underestimated.
[b] T_c: reference epoch of mid-transit that minimizes the correlation with the orbital period. T_{14}: total transit duration, time between the first to last contact; $T_{12} = T_{34}$: ingress/egress time, time between the first and the second, or the third and the fourth contact.
[c] $\zeta/R_\star$ is twice the inverse of the time between the center of the planet crossing the stellar limb during ingress and the center of the planet crossing the stellar limb during egress. We use it as a jump parameter in the MCMC procedure. It is related to $a/R_\star$ via $\zeta/R_\star = a/R_\star(2\pi(1 + e \sin\omega))/(P\sqrt{1-b^2}\sqrt{1-e^2})$ (Bakos et al. 2010).
[d] Values for a quadratic law, adopted from the tabulations by Claret (2004) according to the spectroscopic (SME) parameters listed in Table 7.
[e] Orbital eccentricity parameters derived from the global modeling, and primarily determined by the RV data.
[f] Correlation coefficient between the planetary mass M_p and the radius R_p.
[g] The Safronov number is given by $\Theta = \frac{1}{2}(V_{\rm esc}/V_{\rm orb})^2 = (a/R_p)(M_p/M_\star)$ (see Hansen & Barman 2007).
[h] Incoming flux per unit surface area, averaged over the orbit.

BIC $= \chi^2 + d \log n$, where d is 2 or 4 for the circular and eccentric models, respectively, and n is the number of RV data points (e.g., Kipping et al. 2010). We find that for both HAT-P-32 and HAT-P-33 the circular models have lower BIC values than the models in which the eccentricity is allowed to vary (BIC = 30.5 and 33.8 for the circular and eccentric models

Table 9
Orbital and Planetary Parameters for HAT-P-33b

Parameter	Value[a] Circular	Value Eccentric
Light curve parameters		
P (days)	3.474474 ± 0.000001	3.474474 ± 0.000001
T_c (BJD)[b]	$2455110.92595 \pm 0.00022$	$2455100.50255 \pm 0.00023$
T_{14} (days)[b]	0.1839 ± 0.0005	0.1836 ± 0.0007
$T_{12} = T_{34}$ (days)[b]	0.0195 ± 0.0002	0.0194 ± 0.0002
$a/R_\star$	$6.56^{+0.09}_{-0.12}$	$6.08^{+0.98}_{-0.72}$
$\zeta/R_\star$[c]	12.16 ± 0.03	12.17 ± 0.05
$R_p/R_\star$	0.1058 ± 0.0011	0.1057 ± 0.0011
b^2	$0.106^{+0.001}_{-0.001}$	$0.106^{+0.001}_{-0.001}$
$b \equiv a \cos i/R_\star$	$0.325^{+0.002}_{-0.002}$	$0.325^{+0.002}_{-0.002}$
i (deg)	$87.2^{+0.0}_{-0.1}$	$86.7^{+0.8}_{-1.2}$
Limb-darkening coefficients[d]		
c_1, i (linear term)	0.1762	0.1799
c_2, i (quadratic term)	0.3768	0.3748
c_1, z	0.1260	0.1294
c_2, z	0.3671	0.3656
c_1, g	0.4149	0.4216
c_2, g	0.3327	0.3278
RV parameters		
K (m s^{-1})	82.7 ± 10.8	82.8 ± 12.0
$e \cos(\omega)$[e]	0.000 ± 0.000	0.040 ± 0.078
$e \sin(\omega)$[e]	0.000 ± 0.000	0.073 ± 0.138
e	0.000 ± 0.000	0.148 ± 0.081
ω (deg)	0 ± 0	96 ± 119
RV jitter (m s^{-1})	34.4	36.0
$\alpha_{\rm BS}$[f]	-0.814 ± 0.164	-0.794 ± 0.179
Secondary eclipse parameters		
T_s (BJD)	2455112.663 ± 0.000	2455102.330 ± 0.175
$T_{s,14}$	0.1839 ± 0.0005	0.2090 ± 0.0480
$T_{s,12}$	0.0195 ± 0.0002	0.0230 ± 0.0085
Planetary parameters		
M_p ($M_{\rm J}$)	0.762 ± 0.101	0.763 ± 0.117
R_p ($R_{\rm J}$)	1.686 ± 0.045	1.827 ± 0.290
$C(M_p, R_p)$[g]	0.10	0.34
ρ_p (g cm^{-3})	0.20 ± 0.03	$0.15^{+0.11}_{-0.05}$
$\log g_p$ (cgs)	2.82 ± 0.06	2.75 ± 0.13
a (AU)	0.0499 ± 0.0005	0.0503 ± 0.0011
$T_{\rm eq}$ (K)	1782 ± 28	1838 ± 133
Θ[h]	0.033 ± 0.004	$0.030^{+0.007}_{-0.005}$
$\langle F \rangle$ (10^9 erg s^{-1} cm^{-2})[i]	2.27 ± 0.14	$2.58^{+0.93}_{-0.61}$

Notes.

[a] The eccentricity of HAT-P-33 is poorly constrained. We list separately the parameters obtained when a circular orbit is fixed, and when the eccentricity is allowed to vary. As shown in Section 3.4, the circular orbit model is preferred as the simpler model capable of fitting the observations (the Bayesian Information Criterion is lower for the circular model than the eccentric one). For applications requiring a single set of parameters we thus provisionally suggest adopting the circular orbit parameters; however we note that in this case the parameter uncertainties may be underestimated.

[b] T_c: reference epoch of mid-transit that minimizes the correlation with the orbital period. T_{14}: total transit duration, time between the first to last contact; $T_{12} = T_{34}$: ingress/egress time, time between the first and the second, or the third and the fourth contact.

[c] $\zeta/R_\star$ is twice the inverse of the time between the center of the planet crossing the stellar limb during ingress and the center of the planet crossing the stellar limb during egress. We use it as a jump parameter in the MCMC procedure. It is related to $a/R_\star$ via $\zeta/R_\star = a/R_\star(2\pi(1 + e \sin\omega))/(P\sqrt{1-b^2}\sqrt{1-e^2})$ (Bakos et al. 2010).

[d] Values for a quadratic law, adopted from the tabulations by Claret (2004) according to the spectroscopic (SME) parameters listed in Table 7.

[e] Orbital eccentricity parameters derived from the global modeling, and primarily determined by the RV data.

[f] Parameter describing a linear dependence of the RVs on the BS values.

[g] Correlation coefficient between the planetary mass M_p and radius R_p.

[h] The Safronov number is given by $\Theta = \frac{1}{2}(V_{\rm esc}/V_{\rm orb})^2 = (a/R_p)(M_p/M_\star)$ (see Hansen & Barman 2007).

[i] Incoming flux per unit surface area, averaged over the orbit.

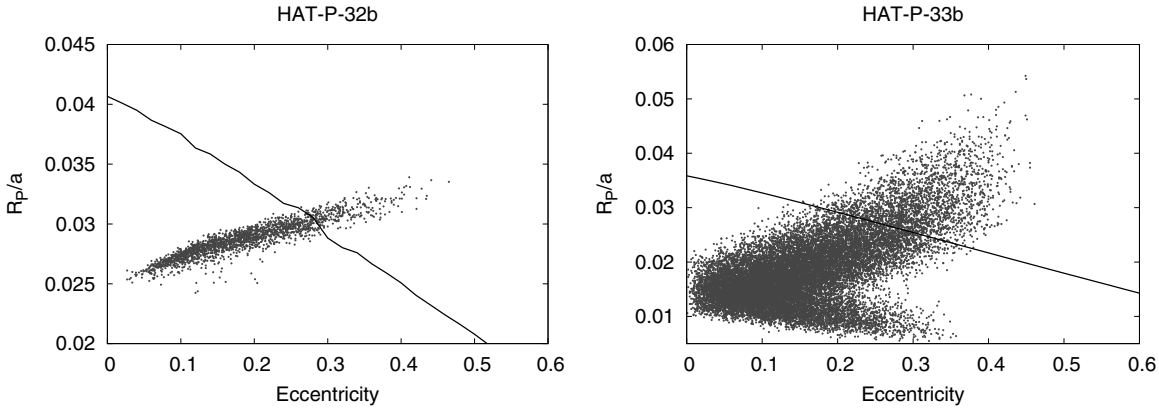

Figure 11. Planet radius normalized to the semimajor axis vs. eccentricity for HAT-P-32b (left) and HAT-P-33b (right). Each point corresponds to a single MCMC parameter realization. The solid lines show the maximum allowed transit-inferred planet radius as a function of eccentricity corresponding to a planet which fills its Roche lobe at periastron (see Appendix). These are calculated using the median mass ratio and argument of periastron for each system. The wiggles seen for HAT-P-32b are due to numerical noise in the calculation.

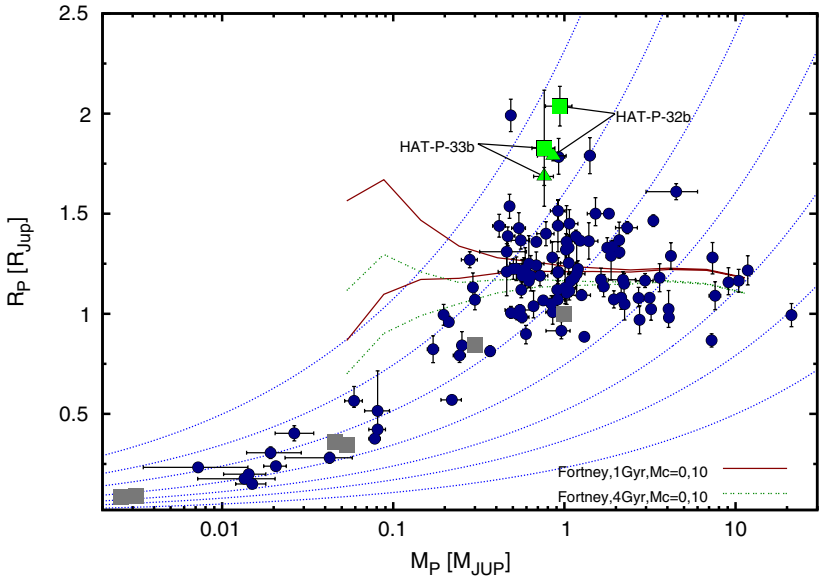

Figure 12. Mass–radius diagram of TEPs. HAT-P-32b and HAT-P-33b are indicated. The triangles indicate the parameters for assumed circular orbits, while the squares indicate the parameters when the eccentricity is allowed to vary. Filled circles are all other TEPs, and filled squares are solar system planets. We also show lines of constant density (dotted lines running from lower left to upper right) and irradiated theoretical planet mass–radius relations from Fortney et al. (2007). We show the relations for core masses of 0 and 10 $M_{\oplus}$ (upper and lower relations) and for planet ages of 1 Gyr and 4 Gyr.

(A color version of this figure is available in the online journal.)

for HAT-P-32, and BIC = 28.3 and 34.0 for the circular and eccentric models for HAT-P-33), indicating that for both systems a circular orbit model is preferred over a model in which the eccentricity is allowed to vary.

Because the resulting planets have large radii (particularly when the eccentricity is allowed to vary), the assumption that each planet has a spherical surface which lies well within its Roche lobe may no longer be valid. In particular the fact that a planet cannot exceed its Roche lobe places an upper limit on the transit-inferred radius of the planet for a given semimajor axis, eccentricity, and mass ratio. Following the procedure described in the Appendix, we impose the constraint that the planet cannot exceed its Roche lobe in determining the parameters and errors for each system. Figure 11 shows an approximation of the constraints on R_p/a and e for each system. In both cases the best-fit solutions are below this limit; however the uncertainties on the parameters (particularly the upper uncertainties on the eccentricities and radii) are reduced by imposing the Roche lobe constraint.

4. DISCUSSION

We have presented the discovery of two planets, HAT-P-32b and HAT-P-33b, which have radii that are among the largest measured to date for all TEPs. Figure 12 shows the location of these two planets on a mass–radius diagram, while Figure 13 shows them on an equilibrium temperature–radius diagram. For each planet the radius determination depends strongly on the eccentricity, which is poorly constrained for both systems due to the high stellar jitters. If HAT-P-32b has a circular orbit, its radius would be $\sim$1.8 $R_{\rm J}$, but it could be as large as $\sim$2.0 $R_{\rm J}$ if the planet is eccentric. HAT-P-33b has a slightly smaller radius of $\sim$1.7 $R_{\rm J}$ if it is on a circular orbit, but its radius could also be larger ($\sim$1.8 $R_{\rm J}$) if it is eccentric. Using the BIC we find that for both systems the assumed circular orbit models are preferred over models where the eccentricity is allowed to vary on the grounds that the circular models provide simpler descriptions of the observations. While we suggest adopting the parameters

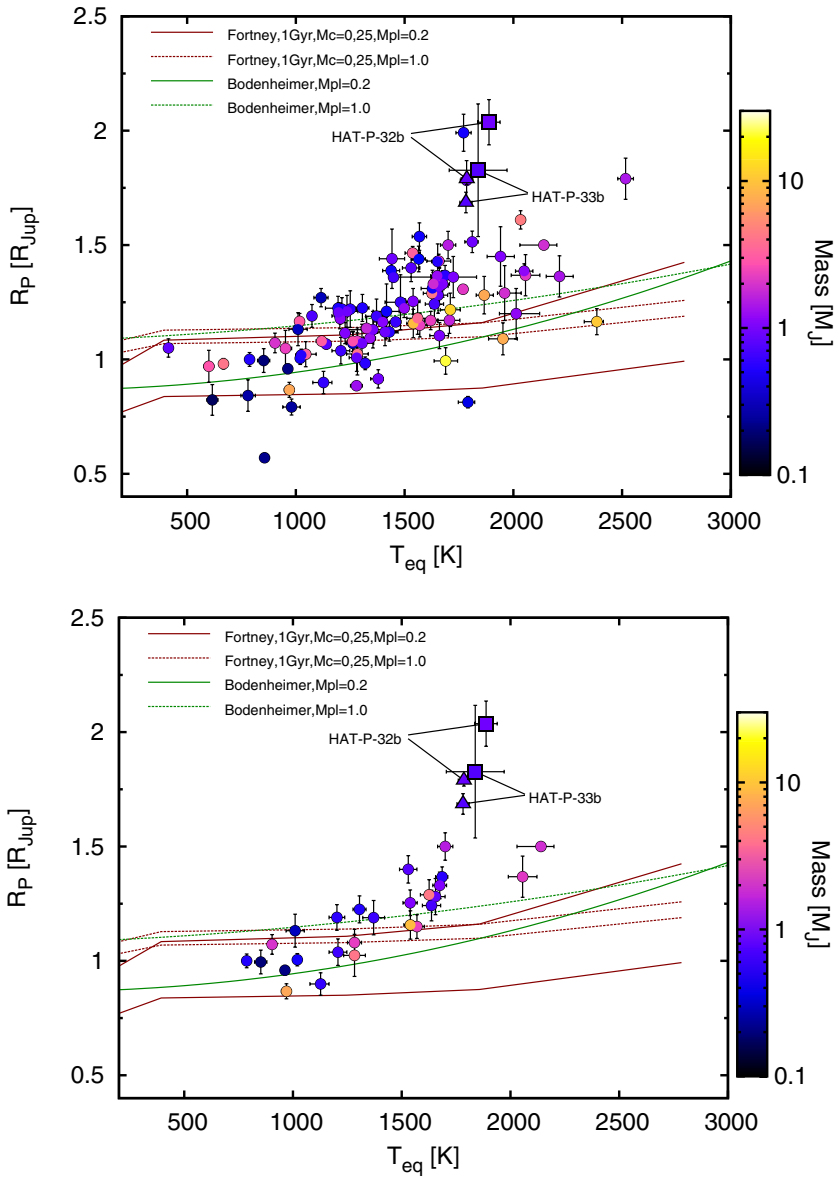

Figure 13. Top: $T_{\rm eq}$–radius diagram of TEPs with $M_p > 0.1\,M_J$. HAT-P-32b and HAT-P-33b are indicated with triangles (circular models) and squares (eccentric models). The shading of the planets indicates their masses. We show theoretical relations from Fortney et al. (2007) and Bodenheimer et al. (2003). We show models for both 0.2 M_J and 1.0 M_J planets, and we show the 0 $M_\oplus$ and 25 $M_\oplus$ core-mass Fortney et al. (2007) models. HAT-P-32b and HAT-P-33b continue the trend of higher $T_{\rm eq}$ planets having larger radii. Bottom: the same as above—here we only show planets discovered by the HATNet survey. The $T_{\rm eq}$–radius correlation is clearly apparent when restricted to this sample of planets, which we take as evidence that the correlation is not due to combining planets found by different surveys that have different selection biases.

(A color version of this figure is available in the online journal.)

based on the assumed circular orbit models, we caution that several eccentric short-period TEPs have been discovered (e.g., XO-3b, Johns-Krull et al. 2008; WASP-14b, Joshi et al. 2009; HAT-P-21b, Bakos et al. 2011), so assuming circular orbits may underestimate the true parameter uncertainties.

There are only four known transiting planets with radii that are comparable to HAT-P-32b or HAT-P-33b. These are WASP-17b ($R = 1.99 \pm 0.08$ R_J; Anderson et al. 2011), WASP-12b ($R = 1.79 \pm 0.09$ R_J; Hebb et al. 2009), TrES-4b ($R = 1.78 \pm 0.09$ R_J; Sozzetti et al. 2009), and Kepler-7b ($R = 1.614 \pm 0.015$ R_J; Demory et al. 2011). These four planets orbit F stars, as do HAT-P-32b and HAT-P-33b. The relatively high luminosities of these stars result in relatively high planet equilibrium temperatures ($T_{\rm eq} > 1600$ K in all cases). The equilibrium temperature in turn is correlated with planet radius (see references in Section 1). Nonetheless, there must be additional factors which cause planets like HAT-P-32b, HAT-P-33b, and WASP-17b to have radii of 1.7–2 R_J with $T_{\rm eq} \sim 1800$ K, while the much hotter planet WASP-18b (2380 K; Hellier et al. 2009) has a much less inflated radius of only 1.165 R_J. One significant difference between WASP-18b and the higher radii planets are the planet masses. While HAT-P-32b, HAT-P-33b, and WASP-17b have sub-Jupiter masses, WASP-18b has a mass of $\sim$10 M_J. As seen in Figure 13 it appears that there may be a mass dependence to the $T_{\rm eq}$–radius relation, with lower mass planets being more strongly impacted by high equilibrium temperature than higher mass planets. A mass dependence of this type has been predicted by several planet inflation mechanisms (e.g., Figure 10 of Guillot 2005; see also Batygin et al. 2011).

Due to the high jitters of the two stars studied in this paper, further high-precision RV observations will not significantly constrain the eccentricities of the planetary systems. A more promising method would be to observe the planetary occultations with the *Spitzer Space Telescope*. Fortunately, both stars are relatively bright, ($K_S \sim 10.0$ mag in both cases) and have expected occultations deeper than 0.1% in both the 3.5 μm and 4.6 μm bandpasses. Thus, we expect that it should be possible to obtain high S/N occultation events (S/N > 10) with *Spitzer* for both systems.

From standard tidal theory we expect the circularization timescales to be much shorter than the $\gtrsim$2 Gyr ages of the systems. Using Equation (1) of Matsumura et al. (2008) and assuming planetary and stellar tidal damping factors of $Q'_p = Q'_\star = 10^6$, the expected circularization timescales are $\sim$3 Myr and $\sim$30 Myr for HAT-P-32b and HAT-P-33b, respectively. We note, however, that Penev & Sasselov (2011) have recently argued that standard tidal theory, which is calibrated from observations of binary stars, significantly overestimates the tidal interaction between planets and stars and thereby underestimates the true circularization timescale. It is possible that a short-period planet may maintain an eccentric orbit for the entire life of the system.

Finally, we note that the difficulty of confirming the planets presented here illustrates the selection bias imposed on transit surveys by the need for RV confirmation. For both planets the HATNet transit detection was clear and robust. This, together with the high S/N box-shaped transits observed with KeplerCam, motivated us to continue obtaining high-precision RVs for these objects despite the initial RVs not phasing with the photometric ephemerides, and the stars showing significant spectral line BS variations. If either target had a shallower, less obviously planet-like transit, it is likely that we would not have continued the intensive RV monitoring necessary for confirmation, and it is also likely that we would not have been able to conclusively rule out blends based on analyzing the light curves. Moreover, if either planet had a significantly lower mass (Saturn mass or smaller), such that the orbital variation could not be detected, it is also likely that the planet would not have been confirmed.

HATNet operations have been funded by NASA grants NNG04GN74G, NNX08AF23G and SAO IR&D grants. Works of G.Á.B. and J. J. were supported by the Postdoctoral Fellowship of the NSF Astronomy and Astrophysics Program (AST-0702843 and AST-0702821, respectively). G.T. acknowledges partial support from NASA grant NNX09AF59G. We acknowledge partial support also from the *Kepler* Mission under NASA Cooperative Agreement NCC2-1390 (PI: D.W.L.). G.K. thanks the Hungarian Scientific Research Foundation (OTKA) for support through grant K-81373. This research has made use of Keck telescope time granted through NOAO (A285Hr, A146Hr, A201Hr, A289Hr), NASA (N128Hr, N145Hr, N049Hr, N018Hr, N167Hr, N029Hr), and the NOAO Gemini/Keck time-exchange program (G329Hr). We gratefully acknowledge F. Bouchy, F. Pont, and the SOPHIE team for their efforts in gathering OHP/SOPHIE observations of HAT-P-33.

APPENDIX

CALCULATING THE TRANSIT-INFERRED RADIUS OF AN ECCENTRIC, ROCHE LOBE FILLING PLANET

The condition that the surface of a planet cannot extend beyond its Roche lobe (assuming the system is *not* an overcontact binary, which is true for the systems considered in this paper since in both cases the inferred stellar radius is well within the stellar Roche lobe for eccentricities that are consistent with the RV curves) sets a maximum limit on its size for a given semimajor axis, eccentricity, and star–planet mass ratio. This in turn places an upper limit on the radius of a planet inferred from a transit measurement. Here, we briefly review how to calculate this constraint.

Following Wilson (1979), the binary potential for the general case of nonsynchronously rotating components on a noncircular orbit is given by

$$\Omega = r^{-1} + q[(D^2 + r^2 - 2r\lambda D)^{-1/2} - r\lambda/D^2] + \frac{1}{2}F^2(1+q)r^2(1-\nu^2). \quad \text{(A1)}$$

The spherical coordinates r, θ, and ϕ (θ is the polar angle) have an origin at the center of one of the binary components (in our case we choose the planet), distance is measured in units of the semimajor axis of the relative orbit, λ and ν are direction cosines ($\lambda = \sin\theta\cos\phi$, $\nu = \cos\theta$), D is the instantaneous separation between the planet and star ($D = 1 - e\cos E$, where e is the eccentricity and E is the eccentric anomaly), q is the mass ratio ($q = M_\star/M_p$ in our case), and F is the synchronicity parameter equal to the ratio of the angular rotation velocity of the component at the origin (the planet in our case) to the "average" angular velocity of the orbit ($2\pi/P$, where P is the orbital period). For an eccentric system the tidal interaction drives the components toward pseudosynchronous rotation, which is between the average angular velocity and the angular velocity at periastron (Hut 1981, Equation (42)):

$$F = \frac{1 + \frac{15}{2}e^2 + \frac{45}{8}e^4 + \frac{5}{16}e^6}{\left(1 + 3e^2 + \frac{3}{8}e^4\right)(1-e^2)^{3/2}}. \quad \text{(A2)}$$

We assume pseudosynchronous rotation for the planet.

The surface of a gas giant planet is expected to follow a surface of constant potential. For the eccentric case the value and shape of the surface potential varies with the orbital phase; in this case Wilson (1979) argues that to a good approximation the volume of the object is constant over the orbit, and suggests a procedure, which we adopt, for finding the surface of a Roche-lobe-filling object at different orbital phases. Because the volume of the Roche lobe is smallest at periastron, it follows that an eccentric planet which fills its Roche lobe will do so only at periastron. The potential Ω_0 corresponding to the Roche lobe of the planet at periastron can be determined by taking $D = 1 - e$ and finding r between 0 and D that minimizes Equation (A1) for $\nu = 0$, $\lambda = 1$. The volume V_0 of this surface can be calculated numerically. We perform a Monte Carlo integration randomly generating points uniformly distributed within a spherical shell with an inner radius r_0 that satisfies the condition $\Omega(r_0, \theta, \lambda) > \Omega_0$ for all θ and λ and an outer radius r_1 that satisfies $\Omega(r_1), \theta, \lambda) < \Omega_0$ for all θ and λ, and taking the volume to be equal to

$$V_0 = \frac{4}{3}\pi\left(r_0^3 + f\left(r_1^3 - r_0^3\right)\right), \quad \text{(A3)}$$

where f is the fraction of generated points with $\Omega > \Omega_0$. The surface potential during transit Ω_1 may then be determined by setting D equal to the appropriate value at transit and finding Ω such that $V(\Omega = \Omega_1) = V_0$. We solve this using a simple bisection search noting that the volume of the Roche

Table 10
Best-fit Parameters for Equation (A5)

Parameter	Value
a_1	0.0033 ± 0.0011
a_2	-0.385 ± 0.016
a_3	-1.673 ± 0.056
a_4	-0.487 ± 0.036
a_5	-0.00222 ± 0.00032
a_6	-0.2927 ± 0.0046
a_7	-1.199 ± 0.017
a_8	0.1397 ± 0.0086
a_9	$-1.434 \times 10^{-3} \pm 6.9 \times 10^{-5}$
a_{10}	-0.30528 ± 0.00097
a_{11}	-0.9238 ± 0.0031
a_{12}	-0.00399 ± 0.00088

lobe potential at transit phase (which can be determined as at periastron) is greater than V_0. Finally, the radius of the planet which would be inferred from a transit observation (corresponding to the radius of a circle with area equal to the projected area of the planet surface potential as viewed by an Earth-bound observer) is given approximately by

$$R_{p,\mathrm{RL}} = \sqrt{yz}, \tag{A4}$$

where $y = r$ such that $\Omega(r, \theta = \pi/2, \phi = \pi/2) = \Omega_1$, $z = r$ such that $\Omega(r, \theta = 0, \phi = 0) = \Omega_1$, and we assume for simplicity an edge-on orbit (which is reasonable for a transiting planet). We have also conducted a Monte Carlo integration to calculate the projected area of the planet surface potential accounting for inclination, and found the difference from the approximation to be negligible (less than 0.1%).

In principle one may apply the Roche lobe constraint in the global modeling of the photometry and RVs by calculating $R_{p,\mathrm{RL}}$ for each set of trial MCMC parameters, and rejecting the trial if it yields $R_p/a > R_{p,\mathrm{RL}}$. In practice this is unwieldy because of the slow numerical integrations required by the above procedure. We therefore searched for an analytic approximation to $R_{p,\mathrm{RL}}$ that depends on the mass ratio q, the eccentricity e, and the argument of periastron ω. We numerically determined $R_{p,\mathrm{RL}}$ over a grid of parameters spanning $10 \leqslant q \leqslant 10^5$, $0 \leqslant e \leqslant 0.5$, and $\pi/2 \leqslant \omega \leqslant 3\pi/2$, and find that the following empirically chosen analytic function reproduces $R_{p,\mathrm{RL}}$ to $\sim$1% accuracy over this parameter range:

$$R_{p,\mathrm{RL}}(q, \omega, e) \approx f_1(q)g_1(\omega)e^2 + f_2(q)g_2(\omega)e + f_3(q)g_3(\omega), \tag{A5}$$

where

$$\begin{aligned}
f_1(q) &= -\exp(a_1 \ln(q)^2 + a_2 \ln(q) + a_3),\\
g_1(\omega) &= a_4 \cos(\omega - \pi/2) + 1,\\
f_2(q) &= -\exp(a_5 \ln(q)^2 + a_6 \ln(q) + a_7),\\
g_2(\omega) &= a_8 \cos(\omega - \pi/2) + 1,\\
f_3(q) &= \exp(a_9 \ln(q)^2 + a_{10} \ln(q) + a_{11}),\\
g_3(\omega) &= a_{12} \cos(\omega - \pi/2) + 1,
\end{aligned}$$

and a_1 through a_{12} are fitted parameters given in Table 10.

REFERENCES

Anderson, D. R., Smith, A. M. S., Lanotte, A. A., et al. 2011, MNRAS, 416, 2108
Bakos, G. Á., Hartman, J., Torres, G., et al. 2011, ApJ, in press (arXiv:1008.3388)
Bakos, G. Á., Kovács, G., Torres, G., et al. 2007, ApJ, 670, 826
Bakos, G. Á., Noyes, R. W., Kovács, G., et al. 2004, PASP, 116, 266
Bakos, G. Á., Torres, G., Pál, A., et al. 2010, ApJ, 710, 1724
Baraffe, I., Chabrier, G., Allard, F., & Hauschildt, P. H. 1998, A&A, 337, 403
Batygin, K., & Stevenson, D. J. 2010, ApJ, 714, L238
Batygin, K., Stevenson, D. J., & Bodenheimer, P. H. 2011, ApJ, 738, 1
Béky, B., Bakos, G. Á., Hartman, J., et al. 2011, ApJ, 734, 109L
Bodenheimer, P., Laughlin, G., & Lin, D. N. C. 2003, ApJ, 592, 555
Bodenheimer, P., Lin, D. N. C., & Mardling, R. A. 2001, ApJ, 548, 466
Burrows, A., Hubeny, I., Budaj, J., & Hubbard, W. B. 2007, ApJ, 661, 502
Butler, R. P., Marcy, G. W., Williams, E., et al. 1996, PASP, 108, 500
Carpenter, J. M. 2001, AJ, 121, 2851
Claret, A. 2004, A&A, 428, 1001
Demory, B. O., Seager, S., Madhusudhan, N., et al. 2011, ApJ, 735, L12
Droege, T. F., Richmond, M. W., & Sallman, M. 2006, PASP, 118, 1666
Enoch, B., Cameron, A. C., Anderson, D. R., et al. 2011, MNRAS, 410, 1631
Etzel, P. B. 1981, in NATO ASI, Photometric and Spectroscopic Binary Systems, ed. E. Carling & Z. Kopal (Dordrecht: Reidel), 111
Faedi, F., Barros, S. C. C., Anderson, D. R., et al. 2011, A&A, 431, A40
Ford, E. 2006, ApJ, 642, 505
Fortney, J. J., Marley, M. S., & Barnes, J. W. 2007, ApJ, 659, 1661
Girardi, L., Bressan, A., Bertelli, G., & Chiosi, C. 2000, A&AS, 141, 371
Guillot, T. 2005, Ann. Rev. Earth Planet. Sci., 33, 493
Guillot, T., Santos, N. C., Pont, F., et al. 2006, A&A, 453, L21
Guillot, T., & Showman, A. P. 2002, A&A, 385, 156
Hansen, B. M. S., & Barman, T. 2007, ApJ, 671, 861
Hartman, J. D., Bakos, G. Á., Kipping, D. M., et al. 2011a, ApJ, 728, 138
Hartman, J. D., Bakos, G. Á., & Torres, G. 2011b, in EPJ Web of Conf. 11, Detection and Dynamics of Transiting Exoplanets, ed. F. Bouchy, R. Díaz, & C. Moutou (France: St. Michel l'Observatoire), 2002
Hebb, L., Collier-Cameron, A., Loeillet, B., et al. 2009, ApJ, 693, 1920
Hellier, C., Anderson, D. R., Collier Cameron, A., et al. 2009, Nature, 460, 1098
Hut, P. 1981, A&A, 99, 126
Isaacson, H., & Fischer, D. 2010, ApJ, 725, 875
Johns-Krull, C. M., McCullough, P. R., Burke, C. J., et al. 2008, ApJ, 677, 657
Joshi, Y. C., Pollacco, D., Collier Cameron, A., et al. 2009, MNRAS, 392, 1532
Kipping, D. M., Bakos, G. Á., Hartman, J., et al. 2010, ApJ, 725, 2017
Kovács, G., Bakos, G. Á., Hartman, J. D., et al. 2010, ApJ, 724, 866
Kovács, G., Bakos, G. Á., & Noyes, R. W. 2005, MNRAS, 356, 557
Kovács, G., Zucker, S., & Mazeh, T. 2002, A&A, 391, 369
Latham, D. W. 1992, in ASP Conf. Ser. 32, IAU Coll. 135, Complementary Approaches to Double and Multiple Star Research, ed. H. A. McAlister & W. I. Hartkopf (San Francisco, CA: ASP), 110
Latham, D. W., Bakos, G. Á., Torres, G., et al. 2009, ApJ, 704, 1107
Laughlin, G., Crismani, M., & Adams, F. C. 2011, ApJ, 729, L7
Liddle, A. R. 2007, MNRAS, 377, L74
Lomb, N. R. 1976, A&SS, 39, 447
Lucy, L. B., & Sweeney, M. A. 1971, AJ, 76, 544
Mandel, K., & Agol, E. 2002, ApJ, 580, L171
Marcy, G. W., & Butler, R. P. 1992, PASP, 104, 270
Matsumura, S., Takeda, G., & Rasio, F. A. 2008, ApJ, 686, L29
Melo, C., Santos, N. C., Gieren, W., et al. 2007, A&A, 467, 721
Nelson, B., & Davis, W. D. 1972, ApJ, 174, 617
Noyes, R. W., Hartmann, L. W., Baliunas, S. L., Duncan, D. K., & Vaughan, A. H. 1984, ApJ, 279, 763
Pál, A., Bakos, G. Á., Torres, G., et al. 2008, ApJ, 680, 1450
Pál, A., Bakos, G. Á., Torres, G., et al. 2010, MNRAS, 401, 2665
Penev, K., & Sasselov, D. 2011, ApJ, 731, 67
Popper, D. M., & Etzel, P. B. 1981, AJ, 86, 102
Press, W. H., & Rybicki, G. B. 1989, ApJ, 338, 277
Press, W. H., Teukolsky, S. A., Vetterling, W. T., & Flannery, B. P. 1992, Numerical Recipes in C: The Art of Scientific Computing (2nd ed.; Cambridge, NY: Cambridge Univ. Press), 640
Press, W. H., Teukolsky, S. A., Vetterling, W. T., & Flannery, B. P. 2007, Numerical Recipes: The Art of Scientific Computing (3rd ed.; Cambridge, NY: Cambridge Univ. Press), 826
Queloz, D., Eggenberger, A., Mayor, M., et al. 2000, A&A, 359, L13
Saar, S. H., Butler, R. P., & Marcy, G. W. 1998, ApJ, 498, L153
Saar, S. H., Hatzes, A., Cochran, W., & Paulson, D. 2003, The Future of Cool-Star Astrophysics: 12th Cambridge Workshop on Cool Stars, Stellar Systems, and the Sun (Boulder, CO: Univ. of Colorado), 12, 694
Scargle, J. D. 1982, ApJ, 263, 835

Schwarz, G. 1978, Ann. Stat., 6, 461
Seager, S., & Mallén-Ornelas, G. 2003, ApJ, 585, 1038
Shporer, A., Bakos, G. Á., Mazeh, T., Kovács, G., & Sipőcz, B. 2009, in IAU Symp. 253, Transiting Planets, ed. F. Pont, D. Sasselov, & M. Holman (Cambridge: Cambridge Univ. Press), 331
Skrutskie, M. F., Cutri, R. M., Stiening, R., et al. 2006, AJ, 131, 1163
Southworth, J., Maxted, P. F. L., & Smalley, B. 2004a, MNRAS, 351, 1277
Southworth, J., Zucker, S., Maxted, P. F. L., & Smalley, B. 2004b, MNRAS, 355, 986
Sozzetti, A., Torres, G., Charbonneau, D., et al. 2009, ApJ, 691, 1145
Torres, G., Boden, A. F., Latham, D. W., Pan, M., & Stefanik, R. P. 2002, AJ, 124, 1716
Torres, G., Fressin, F., Batalha, N. M., et al. 2011, ApJ, 727, 24
Torres, G., Konacki, M., Sasselov, D. D., & Jha, S. 2005, ApJ, 619, 558
Valenti, J. A., & Fischer, D. A. 2005, ApJS, 159, 141
Valenti, J. A., & Piskunov, N. 1996, A&AS, 118, 595
Vaughan, A. H., Preston, G. W., & Wilson, O. C. 1978, PASP, 90, 267
Vogt, S. S., Allen, S. L., Bigelow, B. C., et al. 1994, Proc. SPIE, 2198, 362
Wilson, R. E. 1979, ApJ, 234, 1054
Winn, J. N., Johnson, J. A., Peek, K. M. G., et al. 2007, ApJ, 655, L167
Yi, S. K., Demarque, P., Kim, Y.-C., et al. 2001, ApJS, 136, 417